Physics and Astronomy   College of Arts and Sciences

2011

Scaling Relations and Overabundance of Massive Clusters at Z ≳ 1 from Weak-Lensing Studies with the Hubble Space Telescope

M J. Jee

KS Dawson

H Hoekstra

S Perlmutter

P Rosati

See next page for additional authors

Follow this and additional works at: http://repository.usfca.edu/phys

Part of the Astrophysics and Astronomy Commons, and the Physics Commons

Recommended Citation

Authors

M J. Jee, KS Dawson, H Hoekstra, S Perlmutter, P Rosati, M Brodwin, N Sukuzi, B Koester, M Postman, L Lubin, J Meyers, SA Stanford, K Barbary, F Barrientos, P Eisenhardt, HC Ford, DG Gibank, MD Gladders, A Gonzalez, DW Harris, Xiaosheng Huang, C Lidman, ES Rykoff, D Rubin, and AL Spadafora

SCALING RELATIONS AND OVERABUNDANCE OF MASSIVE CLUSTERS AT $z \gtrsim 1$ FROM WEAK-LENSING STUDIES WITH THE *HUBBLE SPACE TELESCOPE*[*]

M. J. JEE[1], K. S. DAWSON[2], H. HOEKSTRA[3], S. PERLMUTTER[4], P. ROSATI[5], M. BRODWIN[6], N. SUZUKI[4], B. KOESTER[7],
M. POSTMAN[8], L. LUBIN[1], J. MEYERS[4], S. A. STANFORD[1,9], K. BARBARY[4,10], F. BARRIENTOS[11], P. EISENHARDT[12], H. C. FORD[13],
D. G. GILBANK[14], M. D. GLADDERS[7], A. GONZALEZ[15], D. W. HARRIS[2], X. HUANG[4], C. LIDMAN[16], E. S. RYKOFF[4], D. RUBIN[4,10],
AND A. L. SPADAFORA[4]
[1] Department of Physics, University of California, Davis, One Shields Avenue, Davis, CA 95616, USA
[2] Department of Physics and Astronomy, University of Utah, Salt Lake City, UT 84112, USA
[3] Leiden Observatory, Leiden University, Leiden, The Netherlands
[4] E.O. Lawrence Berkeley National Laboratory, 1 Cyclotron Road, Berkeley CA 94720, USA
[5] European Southern Observatory, Karl-Schwarzschild-Strasse 2, D-85748, Garching, Germany
[6] Harvard-Smithsonian Center for Astrophysics, 60 Garden Street, Cambridge, MA 02138, USA
[7] Department of Astronomy and Astrophysics, University of Chicago, Chicago, IL 60637, USA
[8] Space Telescope Science Institute, 3700 San Martin Drive, Baltimore, MD 21218, USA
[9] Institute of Geophysics and Planetary Physics, Lawrence Livermore National Laboratory, Livermore, CA 94550, USA
[10] Department of Physics, University of California Berkeley, Berkeley, CA 94720, USA
[11] Department of Astronomy and Astrophysics, Universidad Catolica de Chile, Santiago, Chile
[12] Jet Propulsion Laboratory, California Institute of Technology, Pasadena, CA 91109, USA
[13] Department of Physics and Astronomy, Johns Hopkins University, 3400 North Charles Street, Baltimore, MD 21218, USA
[14] Department of Physics and Astronomy, University Of Waterloo, Waterloo, Ontario N2L 3G1, Canada
[15] Department of Astronomy, University of Florida, Gainesville, FL 32611-2055, USA
[16] Australian Astronomical Observatory, P.O. Box 296, Epping NSW 1710, Australia

ABSTRACT

We present weak gravitational lensing analysis of 22 high-redshift ($z \gtrsim 1$) clusters based on *Hubble Space Telescope* images. Most clusters in our sample provide significant lensing signals and are well detected in their reconstructed two-dimensional mass maps. Combining the current results and our previous weak-lensing studies of five other high-z clusters, we compare gravitational lensing masses of these clusters with other observables. We revisit the question whether the presence of the most massive clusters in our sample is in tension with the current ΛCDM structure formation paradigm. We find that the lensing masses are tightly correlated with the gas temperatures and establish, for the first time, the lensing mass–temperature relation at $z \gtrsim 1$. For the power-law slope of the $M-T_X$ relation ($M \propto T^\alpha$), we obtain $\alpha = 1.54 \pm 0.23$. This is consistent with the theoretical self-similar prediction $\alpha = 3/2$ and with the results previously reported in the literature for much lower redshift samples. However, our normalization is lower than the previous results by 20%–30%, indicating that the normalization in the $M-T_X$ relation might evolve. After correcting for Eddington bias and updating the discovery area with a more conservative choice, we find that the existence of the most massive clusters in our sample still provides a tension with the current ΛCDM model. The combined probability of finding the four most massive clusters in this sample after the marginalization over cosmological parameters is less than 1%.

Key words: cosmology: observations – dark matter – galaxies: clusters: general – galaxies: high-redshift – gravitational lensing: weak – X-rays: galaxies: clusters

Online-only material: color figures

1. INTRODUCTION

Gravitationally-bound systems have been the main objects of study by astronomers throughout history because they are observationally identified as discrete entities in the universe. Galaxy clusters, the largest among these, are believed to be also the last systems detached from the Hubble expansion. Studying galaxy clusters provides unique opportunities to test our structure formation paradigm, understand gas physics, infer the properties of dark matter, investigate cluster galaxy evolution, and constrain cosmological parameters.

The formalism for the last of these, i.e., the use of clusters for cosmology, was pioneered by Press & Schechter (1974), who realized that under the assumption of Gaussian primordial density fluctuation the fraction of mass in halos more massive than the threshold M is related to the fraction of the volume in which the smoothed initial density field is above some threshold density contrast δ_c. This simple, but ingenious, approach has been shown to work well in comparison with numerical simulations. Since this early work, many authors have extended the formalism to provide better agreement with the recent state-of-the-art numerical simulations.

The number of clusters of a given mass, or the mass function, in the local universe constrains the combined properties of the matter density and its fluctuation $\Omega_M \sigma_8^{0.5}$ (e.g., Bahcall & Cen 1993; Pierpaoli et al. 2001; Reiprich & Böhringer 2002, and references therein) whereas the evolution of the mass function breaks this degeneracy (e.g., Bahcall & Fan 1998). Therefore, there has been continuous effort to extend our knowledge of the cluster mass function to higher and higher redshift regimes.

Table 1
Details of *HST* Observations

Cluster Name	Redshift	R.A. (hh mm ss)	Decl. (° ′ ″)	F775W Exp. (s)	F850LP Exp. (s)	n_{bg} (arcmin^{-2})	Prop. ID
XMMXCS J2215−1738	1.46	22 15 59	−17 37 58	3320	16935	85	10496
XMMU J2205−0159	1.12	22 05 50	−01 59 30	4535	11380	77	10496
XMMU J1229+0151	0.98	12 29 29	+01 51 22	4110	10940	99	10496
WARPS J1415+3612	1.03	14 15 11	+36 12 04	2425	9920	78	10496
ISCS J1432+3332	1.11	14 32 29	+33 32 48	4005	12440	115	10496
ISCS J1429+3437	1.26	14 29 18	+34 37 25	2670	15600	81	10496
ISCS J1434+3427	1.24	14 34 28	+34 26 22	2685	13320	84	10496
ISCS J1432+3436	1.35	14 32 38	+34 36 49	2235	8940	81	10496
ISCS J1434+3519	1.37	14 34 46	+35 19 45	1920	11260	70	10496
ISCS J1438+3414	1.41	14 38 09	+34 14 19	2155	10620	76	10496
RCS 0220−0333	1.03	02 20 55	−03 33 10	2955	14420	96	10496
RCS 0221−0321	1.02	02 21 41	−03 21 47	2015	13360	79	10496
RCS 0337−2844	1.1	03 37 50	−28 44 28	1560	12885	67	10496
RCS 0439−2904	0.95	04 39 38	−29 04 55	2075	15530	81	10496
RCS 2156−0448	1.07	21 56 42	−04 48 04	2060	5440	50	10496
RCS 1511+0903	0.97	15 11 03	+09 03 15	2075	7120	65	10496
RCS 2345−3632	1.04	23 45 27	−36 32 50	4450	9680	103	10496
RCS 2319+0038	0.91	23 19 53	+00 38 13	2400	6800	61	10496
XLSS J0223−0436	1.22	02 23 03	−04 36 18	3380	14020	97	10496
RDCS J0849+4452	1.26	08 48 56	+44 52 00	15630	34840	180	9919 and 10496
RDCS J0910+5422	1.11	09 10 44	+54 22 08	9825	25380	148	9919 and 10496
RDCS J1252−2927	1.23	12 52 54	−29 27 17	29945	57070	165	9290 and 10496

During the last decade, many ongoing surveys have increased the number of known $z \gtrsim 1$ clusters by many factors (e.g., Eisenhardt et al. 2008; Boehringer et al. 2006; Gladders & Yee 2005). Therefore, it is now possible to study the evolution of the mass function across a large range of redshifts. Such a study can not only provide an important check to the results obtained thus far from lower redshift samples, but also enable a critical test on the primordial non-Gaussianity (e.g., Jimenez & Verde 2009; Sartoris et al. 2010).

Without question, one of the most crucial issues is the accurate derivation of masses for high-redshift clusters. Indirect approaches, i.e., the estimation from velocity dispersion, X-ray properties, or Sunyaev–Zel'dovich observations, require assumptions on the dynamical state of the clusters and/or the mass versus mass proxy calibration. By contrast, gravitational lensing is a unique tool for obtaining the cluster mass without relying on any dynamical assumption. However, because this method requires expensive, high-resolution observations from space, it is not practical, if not impossible, to perform a lensing analysis for complete samples. Instead, it is much more feasible to apply the technique to a subset of the sample and to use the results to calibrate the relation between masses and their proxies.

In this paper, we present weak-lensing analysis of 22 $z \gtrsim 1$ clusters based on *Hubble Space Telescope* (*HST*) images. Our detailed study of these clusters via their weak gravitational lensing signal will provide the aforementioned, invaluable calibration between weak-lensing masses and other observables. In addition, the most massive among these allow us to investigate the behavior of the high end of the mass function (Hoyle et al. 2011; Holz & Perlmutter 2010). The 22 clusters were discovered in different surveys, and do not represent a complete sample, implying that any significant excess of massive clusters (beyond the sample fluctuation) would in fact underestimate the difference between observation and theory. In order to complement our sample for the investigation of the mass and mass-observable relation and the implication for the cosmology,

we include five other high-redshift clusters that were previously studied via lensing.

The structure of this paper is as follows. In Section 2, we describe our Advanced Camera for Surveys (ACS) data. The method and the weak-lensing mass reconsruction for the 22 clusters are presented in Section 3. Section 4 compares the lensing measurements with other cluster properties for the combined sample of 27 clusters and presents the mass–temperature relation (*M–T*) at $z > 1$. We investigate the abundance of the most massive clusters in our study relative to the theoretical expectations within the current paradigm of the structure formation in Section 5 before we conclude in Section 6. Discussions on the details of our corrections to shape measurements including point-spread function (PSF) and charge transfer inefficiency (CTI) are deferred to Appendices A and B, respectively.

We assume $(\Omega_M, \Omega_\Lambda, h) = (0.3, 0.7, 0.7)$ for cosmology unless explicitly stated otherwise. All the quoted uncertainties are at the 1σ ($\sim 68\%$) level.

2. OBSERVATIONS

The 22 $z \gtrsim 1$ clusters were observed with ACS/WFC using the F775W and F850LP filters (hereafter referred to i_{775} and z_{850}, respectively) as part of the *HST* Cluster Supernova Survey (GO-10496, PI: Perlmutter) during the period of 2005 July–2006 November (see Dawson et al. 2009). Three clusters among these were also observed as part of Guaranteed Time Observation 9290 and 9919 (PI: Ford) during the periods of 2002 May–June and 2004 February–March. Table 1 summarizes the exposure times of the 22 clusters in i_{775} and z_{850}.

2.1. ACS Data Reduction

Our reduction started with the FLT images, which are the products of the standard STScI CALACS pipeline (Hack et al. 2003). We used the "apsis" pipeline (Blakeslee et al. 2003) to determine shift and rotation, correct geometric distortion, remove

cosmic rays, and create final mosaic images. The determination of the shift and rotation between different pointings is the most critical step among these for a weak-lensing analysis because any potential misalignment induces a coherent distortion of object shapes, mimicking gravitational lensing signals. The "apsis" pipeline uses high signal-to-noise (S/N) astronomical objects iteratively to measure and refine the alignment through the "match" program developed by Richmond (2002). We find that the average uncertainties for shift and rotation are ∼0.02 pixels and ∼0″.2, respectively, and thus the systematics, if any, due to the alignment errors is negligible. The Lanczos3 (windowed sinc function) kernel was used for drizzling (Fruchter & Hook 2002) with the native 0″.05 pixel scale of ACS/WFC.

2.2. Object Detection and Source Selection

A detection image was created for each cluster by weight averaging the two passband images via apsis. Then, SExtractor (Bertin & Arnouts 1996) was run in dual image mode so that objects were identified from the detection image while photometry was measured on an individual filter. This provides common isophotal areas to both filters, which enables a robust object color measurement. We filtered the detection image with a Gaussian kernel that approximately matches the PSF of the instrument before looking for five or more contiguous pixels above 1.5 times the sky rms. Although our criteria were experimentally determined to minimize the return of false detections by the software, inevitably manual identification of spurious detections (e.g., saturated stars, diffraction spikes, uncleaned cosmic rays near field boundaries, H II regions inside nearby galaxies, etc.) is always required. We divided the 22 clusters into several groups and a few authors were assigned to each group to carry out this manual procedure. A possible concern is whether or not different groups might have non-negligible biases in this false object identification, which may propagate into cluster mass determination. To examine the possibility of bias in the manual procedure, several clusters were randomly selected by one author and compared to the two false object catalogs created by this author and others. We find that about ∼60% of false objects are shared by the two catalogs, and the disagreement is mostly attributed to very faint objects, whose fluxes are just above the sky background. Because these extremely faint objects were discarded anyway by our magnitude and shape measurement error criteria, the resulting difference in mass estimation and two-dimensional mass reconstruction is far below statistical errors.

We define source galaxies as objects whose $i_{775}-z_{850}$ colors are bluer than the color of the red sequence in each cluster while their total z_{850} magnitudes (MAG_AUTO) are fainter than $z_{850} = 24$. We also require the source galaxies to have ellipticity measurement error less than 0.25. The total exposure times for the 22 clusters vary substantially and thus, so does the number density of source galaxies as shown in Table 1.

2.3. Shape Measurement

Our shape measurement method is detailed in Jee et al. (2009). Briefly, we fit a PSF-convolved elliptical Gaussian function to source galaxies to determine their semi-major and -minor axes. Convolution with an elliptical Gaussian is required to measure galaxies' ellipticity before photons reach the instrument. Because an elliptical Gaussian profile is not an unbiased representation of true galaxies, the measurement inevitably introduces a bias. On average, the bias is toward underestimation of ellipticity because a Gaussian profile is steeper than that of real objects;

more extended objects are subject to larger underestimates of ellipticity. In future analyses, it may be worth experimenting with more generalized functional forms and examining the effect based on simulated images. Nevertheless, we stress that the amount of bias induced by the current shape measurement is small and to first order was corrected here using the simulation results of Jee et al. (2007a), which shows a ∼6% bias for $\gamma \gtrsim 0.5$.

We model the PSF using our library constructed from stellar field observations (Jee et al. 2007a). In order to find the matching PSF template, we use ∼10 high S/N stars present in each cluster field. This matching is done for each visit, and the final PSF model is obtained after the model for each visit is shifted, rotated, and stacked. The mean residual ellipticity is less than ∼0.01, and this level of accuracy is sufficient for the current cluster lensing analysis. The detailed results for each cluster can be found in Appendix A.

Together with the PSF, CTI may be a potential source of systematics in weak lensing. For bright stars, the trailing from deferred charges is visually apparent. We quantify the effect using cosmic rays and warm pixels, and find that the effect on the ellipticity of the galaxies that we use to extract the signal is in fact much less than the statistical noise set by the finite number of galaxies. Thus, we confirm our previous argument (Jee et al. 2009) that the ACS CTI effect is negligible for cluster lensing analysis although it is a critical source of systematics in cosmic shear studies. We present the details in Appendix B.

3. WEAK-LENSING ANALYSIS

3.1. Mass Estimation and Two-dimensional Mass Reconstruction

In the weak-lensing regime, the characteristic length of the lensing signal variation is larger than the object size. Thus, the resulting shape distortion can be linearized as follows:

$$\mathbf{A}(\mathbf{x}) = \delta_{ij} - \frac{\partial^2 \Psi(\mathbf{x})}{\partial x_i \partial x_j} = \begin{pmatrix} 1 - \kappa - \gamma_1 & -\gamma_2 \\ -\gamma_2 & 1 - \kappa + \gamma_1 \end{pmatrix}, \quad (1)$$

where $\mathbf{A}(\mathbf{x})$ is the transformation matrix $\mathbf{x}' = \mathbf{A}\mathbf{x}$, which relates a position $\mathbf{x}$ in source plane to a position $\mathbf{x}'$ in image plane, and Ψ is the two-dimensional lensing potential. The convergence κ is the surface mass density in units of critical surface mass density

$$\Sigma_c = \frac{c^2}{4\pi G} \frac{D(z_s)}{D(z_l)D(z_l, z_s)}, \quad (2)$$

where $D(z_s)$, $D(z_l)$, and $D(z_l, z_s)$ are the angular diameter distance from the observer to the source, from the observer to the lens, and from the lens to the source, respectively. The convergence κ and the shears $\gamma_{1(2)}$ are related to the lensing potential Ψ via

$$\kappa = \frac{1}{2}(\psi_{11} + \psi_{22}), \quad \gamma_1 = \frac{1}{2}(\psi_{11} - \psi_{22}),$$
$$\text{and} \quad \gamma_2 = \psi_{12} = \psi_{21}, \quad (3)$$

where the subscripts on $\psi_{i(j)}$ denote partial differentiation with respect to $x_{i(j)}$.

A useful quantity to estimate masses is the reduced tangential shear defined by

$$g_T = \langle -g_1 \cos 2\phi - g_2 \sin 2\phi \rangle, \quad (4)$$

where ϕ is the position angle of the object with respect to the cluster center and g is the reduced shear $\gamma/(1-\kappa)$ (valid only in the weak-lensing regime). This reduced tangential shear profile informs us of how the mass density of the lens changes as a function of radius. Of course, without any lensing signal, the resulting shear profile should vanish with fluctuations consistent with shot noise.

Hoekstra (2001, 2003) demonstrates that a cosmic shear (lensing by large-scale structure, LSS) is an important limiting factor in the accuracy of cluster masses derived from the cluster tangential shears. Following the formalism of Hoekstra (2003), we estimate that the cosmic shear contribution on average is $\gamma \sim 0.01$ for our sample. Although this is small compared to the shot noise set by the finite number of source galaxies, we include the effect in our final mass uncertainty.

A potential ambiguity is the choice of the cluster center when there is disagreement between centroids determined from the distribution of cluster galaxies, lensing mass peaks, and X-ray emission. If we adopt a location that maximizes the amplitude of the tangential shear or a peak in the convergence map as the cluster center, the derived mass will be always biased high. Fortunately, in previous high S/N weak-lensing studies, where the number density of background galaxies is high (>120 per square arcmin), the weak-lensing mass peaks are in good spatial agreement with cluster galaxies. However, in many cases the X-ray peaks are conspicuously offset, indicative of merging activity or the collisional properties of the intracluster medium (ICM). In this paper, we adopt the centroid defined by the cluster galaxies as the center for the construction of the tangential shear profile. For the clusters in our sample where the statistical significance of the lensing signal is high, these centroids also agree well with the mass peaks. In several cases, where lensing signal is weak (the cluster is not massive and/or the image is not sufficiently deep), we occasionally observe rather large ($>20''$) offsets between mass and galaxies. The choice of centroid will lead to an underestimate of the cluster mass if the offsets reflect real features in the system. We do not use the inner most data points in our mass estimation because the tangential shears at very small radii are highly sensitive to the centroid choice. Furthermore, both observationally and theoretically, it is not clear how the cluster mass profile behaves near the center.

There are two popular ways of deriving the lensing mass from tangential shear: aperture-mass densitometry (Fahlman et al. 1994) and parameterized model fitting. Aperture-mass densitometry is useful when one attempts to estimate the total projected mass within some aperture radius without requiring an assumption on the behavior of the cluster mass profile. However, this approach is not practical for the current data set, which in most cases provides only $\sim 3' \times 3'$ areas smaller than the virial radii of the clusters. Therefore, we use the second method to derive the cluster masses. This method determines the parameters of analytic halo models by comparing the observed tangential shears with the expected values. Of course, a scatter is introduced because the real cluster profile is different from the model. Nevertheless, many studies show that this parametric approach gives consistent results with the values obtained by the former (e.g., Jee et al. 2005a; Hoekstra 2007).

We employ two kinds of halo models: singular isothermal sphere (SIS) and Navarro–Frenk–White (NFW; Navarro et al. 1997) profiles. Although the SIS profile is considered inappropriate at large radii (many lines of evidence suggest the mass density drops faster than $1/r^2$), the resulting parameter can be conveniently translated to the Einstein radius θ_E or the velocity dispersion σ_v of the system. We use this predicted velocity dispersion to compare with the dynamical value. When we fit NFW profiles, it is assumed that the cluster virial mass M_{200} (the total mass at the radius inside of which the mean density is 200 times the critical density of the universe at the cluster redshift) is tied to the concentration c via the following relation from Duffy et al. (2008):

$$c = 5.71 \left(\frac{M_{200}}{2 \times 10^{12} \, h^{-1} \, M_\odot} \right)^{-0.084} (1+z)^{-0.47}. \quad (5)$$

Therefore, effectively, our NFW model is described by a single parameter. The relation between projected mass density and observed shear is simple for SIS with an Einstein radius r_E: $\kappa = 0.5 r_E/r$ and $g = \kappa/(1-\kappa)$ (in the weak-lensing regime). For NFW, the relation is rather complicated, and we refer readers to Bartelmann (1996). We present tangential shears and fitting results for individual clusters in Figure 1.

In principle, the two-dimensional projected mass distribution κ can be obtained by convolving the shear γ as follows (Kaiser & Squires 1993):

$$\kappa(\mathbf{x}) = \frac{1}{\pi} \int D^*(\mathbf{x} - \mathbf{x}') \gamma(\mathbf{x}') d^2\mathbf{x}, \quad (6)$$

where $D(\mathbf{x}) = -1/(x_1 - ix_2)^2$ is the convolution kernel. However, the direct application of Equation (6) gives rises to some practical problems. First, the ellipticity of individual galaxies should be smoothed, and we do not know the optimal smoothing scale beforehand. Second, the smoothed galaxy ellipticity gives only an estimate for the reduced shear $g = \gamma/(1-\kappa)$. Third, the relation $g = \gamma/(1-\kappa)$ is only valid in the $|\gamma/(1-\kappa)| < 1$ regime. Fourth, it is not obvious how to weight shape measurement noise properly via Equation (6).

Certainly, a more robust two-dimensional mass reconstruction algorithm is required to account for the aforementioned subtleties and minimize numerous artifacts. Many suggestions are present in the literature (Bridle et al. 1998; Seitz et al. 1998), and the consensus is that a reliable mass reconstruction should be achieved through iterations. In addition, it is desirable to use the ellipticity of individual galaxies rather than the smoothed values so as to reveal small-scale, but significant, features. In the present paper, we reconstruct two-dimensional mass maps using the entropy-regularized, maximum likelihood code of Jee et al. (2007a). This method of mass reconstruction accounts for the aforementioned subtleties and is effective in revealing low-contrast structures. We present our mass reconstructions in Figures 2–23. Results on individual clusters are discussed in Section 3.3.

3.2. Redshift Estimation of Source Galaxies

Because Σ_c scales as $\propto D(z_s)/[D(z_l)D(z_l, z_s)]$ (Equation (2)), the mass density unit rises sharply as the redshift of the lens approaches that of the source. Thus, in the weak-lensing analysis of high-redshift clusters, small errors in our estimate of the source redshift distribution result in large errors in the translation of the signal into the physical unit. For example, a 10% systematic uncertainty in the effective source redshift leads to 1%–2% error in mass for a $z = 0.2$ object (e.g., A1689). The same amount of uncertainty would give $\sim 30\%$ error for the mass of a $z = 1.4$ lens (e.g., XMM2235–2557).[17]

---

[17] The exact value also depends on the depth of the image, which determines how many distant galaxies are resolved. Here we assume ~ 4 orbit integration with *HST*/ACS.
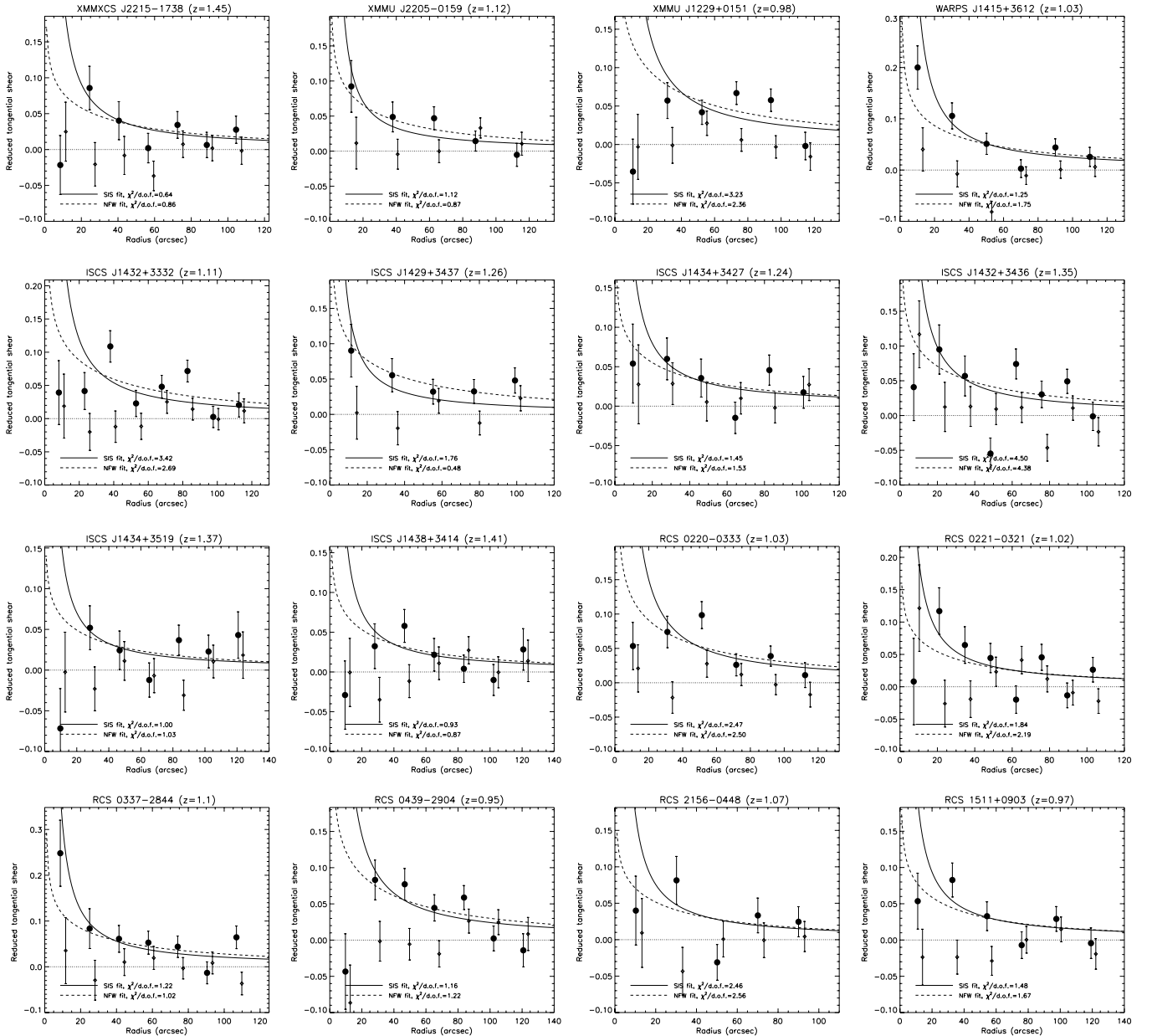
Figure 1. Reduced tangential shears for 22 high-redshift clusters. Filled and open circles represent the tangential shear and $45°$ rotation test results, respectively.

We estimate the redshift distribution of the source population using the publicly available Ultra Deep Field (UDF) photometric redshift catalog (Coe et al. 2006). The ultra deep images in six filters from F435W to F160W provide unparalleled high-quality photometric redshift information well beyond the limiting magnitude of the cluster images that we analyze here. The catalog has been extensively used in our previous studies (e.g., Jee et al. 2009), and thus we only briefly summarize the procedure.

First, we bin our source galaxies in 0.5 mag intervals. Next, we randomly draw the galaxies that match the selection criteria of each bin from the UDF photo-z catalog. Finally, we combine these simulated catalogs for all bins to create the redshift catalog for the entire source population. Because the UDF is much deeper than the cluster images and also because there is sample variance, it is important to take into account the difference in number density in this step. Consequently, we are utilizing the magnitude–color–redshift relation measured in the UDF data,

rather than simplistically imposing the UDF redshift distribution on our images, which would cause much greater systematics.

As noted in Jee et al. (2009), the total error in z_{eff} due to the sample variance, the resampling error, and the difference among the photo-z estimation codes is $\delta z_{eff} \simeq 0.06$. This causes an $\sim11\%$ ($\sim3\%$) uncertainty in mass for a $z \sim 1.4$ ($z \sim 0.9$) cluster. We include these errors in our final uncertainty. The assumption that there exists a single source plane while in reality each source galaxy is at a different redshift also creates a bias in the interpretation of the lensing signal. We correct this bias to first order using the equation derived by Seitz & Schneider (1997).

3.3. Notes on Individual Clusters

We here comment on specific features in the measurement of each cluster. All of the key numbers are summarized in Table 2.
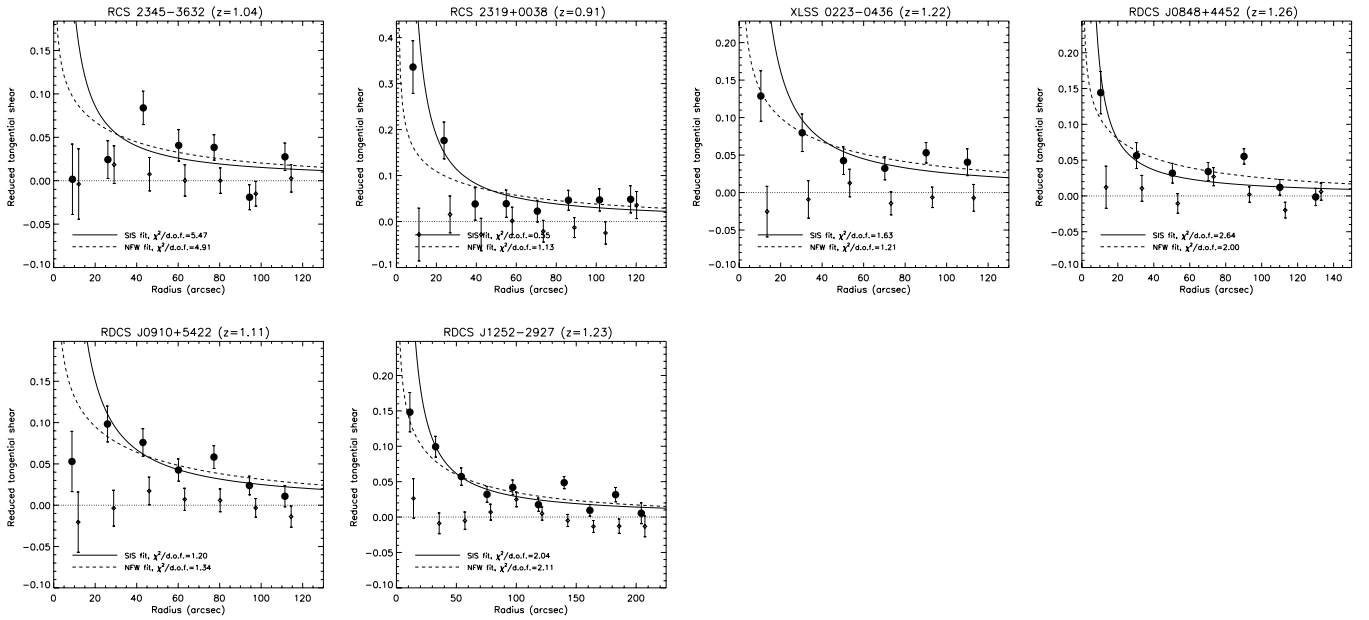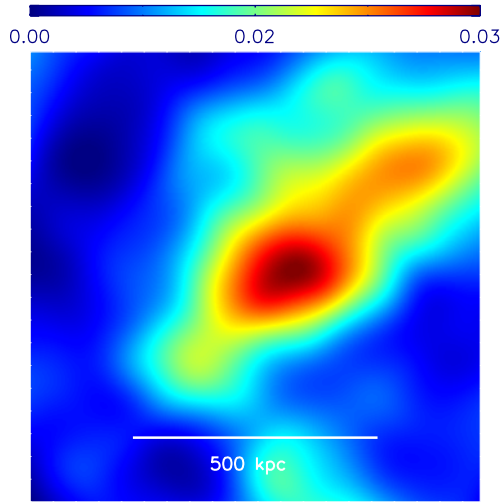
Figure 1. (Continued)

Figure 2. XMMXCS J2215−1738 mass map. The left panel displays the mass reconstruction, whose color represents the mass density. The mass-sheet degeneracy is not broken here, and thus the scale is arbitrary. On the right panel, we overlay the mass contours on the pseudo-color composite created by combining the i_{775} and z_{850} images. The green "X" symbol marks the location of the X-ray peak in the *Chandra* image. Spectroscopically confirmed members are encircled in red.
(A color version of this figure is available in the online journal.)

3.3.1. XMMXCS J2215−1738 (z = 1.46)

XMMXCS2215−1738 was the highest redshift cluster spectroscopically confirmed (Stanford et al. 2006) until the recent discovery of ClG J0218.3−0510 at $z = 1.62$ (Papovich et al. 2010). Assuming no significant point-source contamination in the archival *XMM-Newton* data, Stanford et al. (2006) obtained a temperature of $T_X = 7.4^{+2.7}_{-1.8}$ keV with a bolometric luminosity of $L_X = 4.4^{+0.8}_{-0.6} \times 10^{44}$ erg s^{-1}. Hilton et al. (2010) reported significantly lower values $T_X = 4.1^{+0.6}_{-0.9}$ keV and $L_X = 2.92^{+0.24}_{-0.35} \times 10^{44}$ erg s^{-1} based on a joint analysis of *Chandra* and *XMM-Newton* data, which enable them to remove the point-source contamination from the diffuse component. Assuming an isothermal β model with $\beta = 0.63$ and $r_c = 52$ kpc, the temperature $T_X = 4.1^{+0.6}_{-0.9}$ keV translates into $M_{200} = 2.0^{+0.5}_{-0.6} \times 10^{14} M_\odot$.

We initially considered a weak-lensing study of XMMXCS2215−1738 to be highly challenging because of the low X-ray mass, high-redshift, and relatively shallow depth of the F775W image, where we measure galaxy shapes. However, the cluster is clearly detected in our two-dimensional mass reconstruction, which shows the mass centroid in good spatial agreement with the cluster members and the X-ray centroid (Figure 2). The weak-lensing mass of the cluster is $M_{200} = 4.3^{+3.0}_{-1.7} \times 10^{14} M_\odot$, a factor of two higher than the X-ray estimate (however, both results are marginally consistent).

The predicted velocity dispersion 942^{+111}_{-126} km s^{-1} is consistent with the spectroscopically measured value of 710 ± 110 km s^{-1} derived from 31 members within R_{200} (Hilton et al. 2010); interestingly, if all 44 members were used, the velocity dispersion increases to 890 ± 110 km s^{-1}, giving a better agreement with the lensing result.
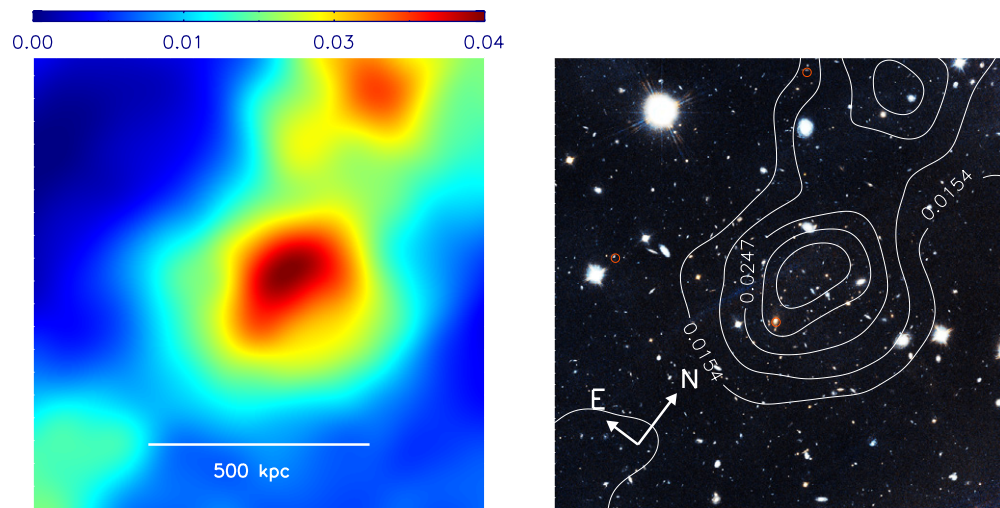
6

Figure 3. Same as Figure 2 but for XMMU J2205−0159.

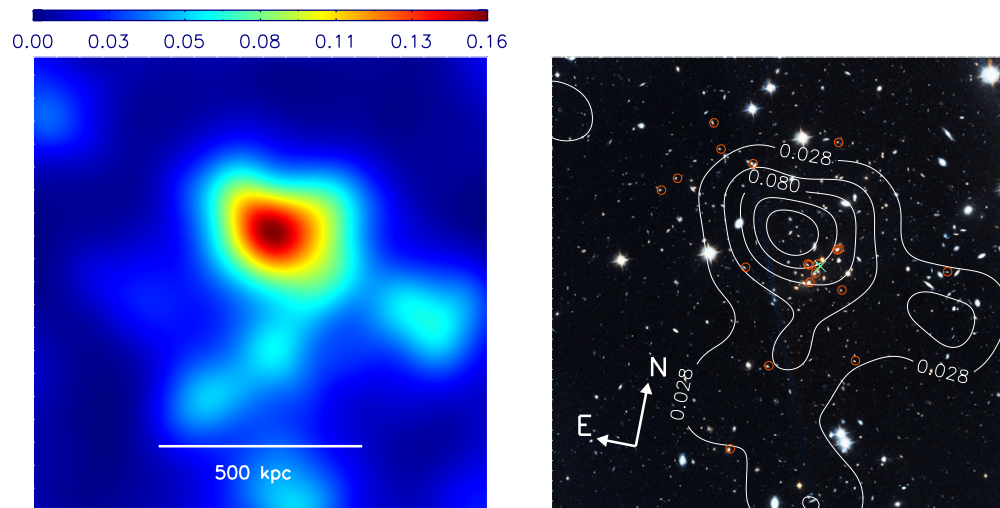(A color version of this figure is available in the online journal.)

Figure 4. Same as Figure 2 but for XMMU J1229+0151.

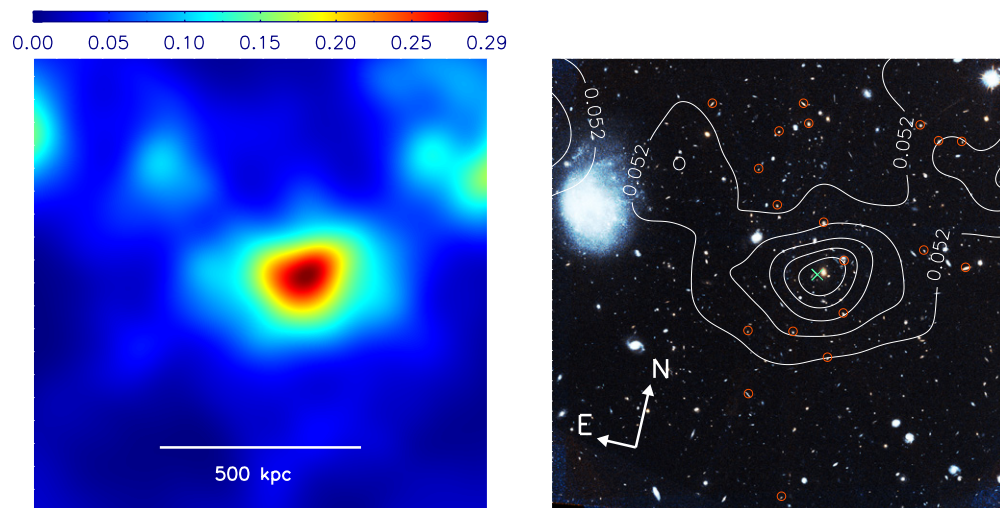(A color version of this figure is available in the online journal.)

Figure 5. Same as Figure 2 but for WARPS J1415+3612.

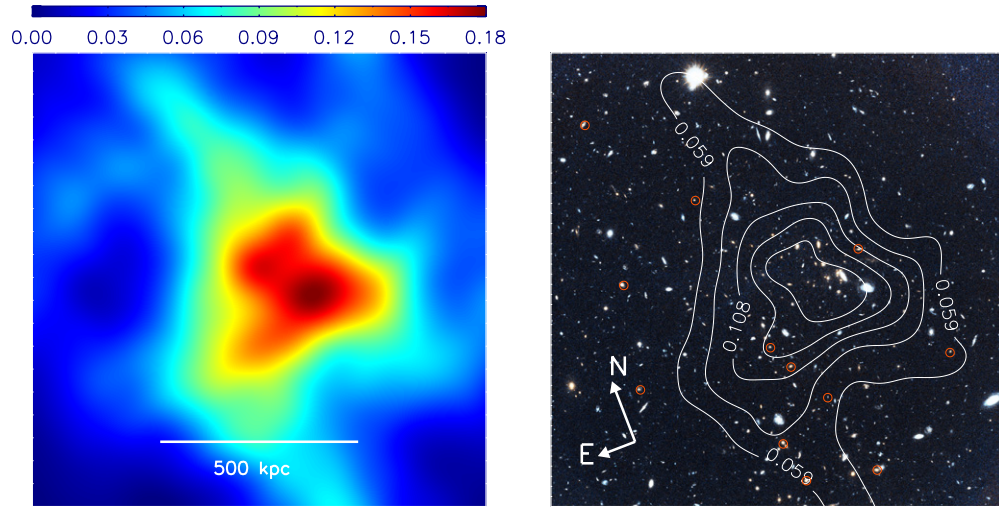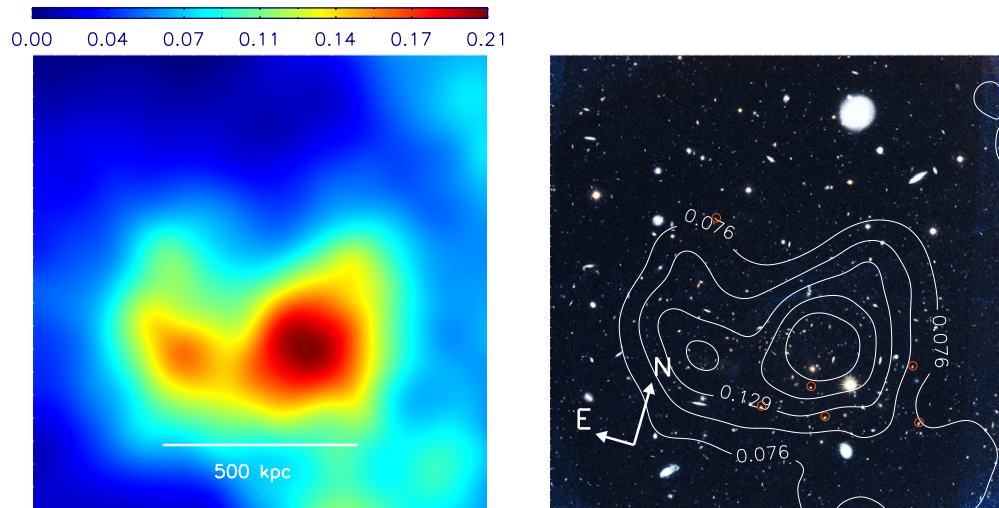(A color version of this figure is available in the online journal.)

Figure 6. Same as Figure 2 but for ISCS J1432+3332.
(A color version of this figure is available in the online journal.)

Figure 7. Same as Figure 2 but for ISCS J1429+3437.
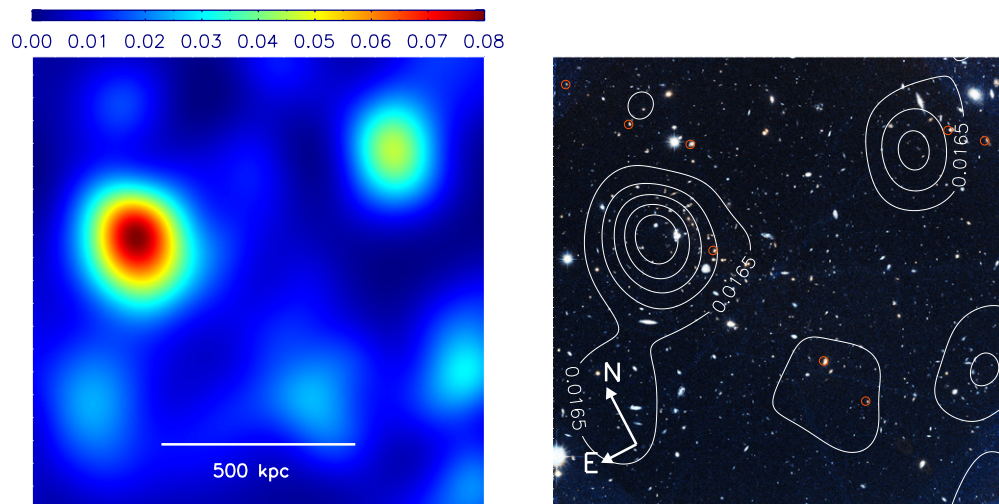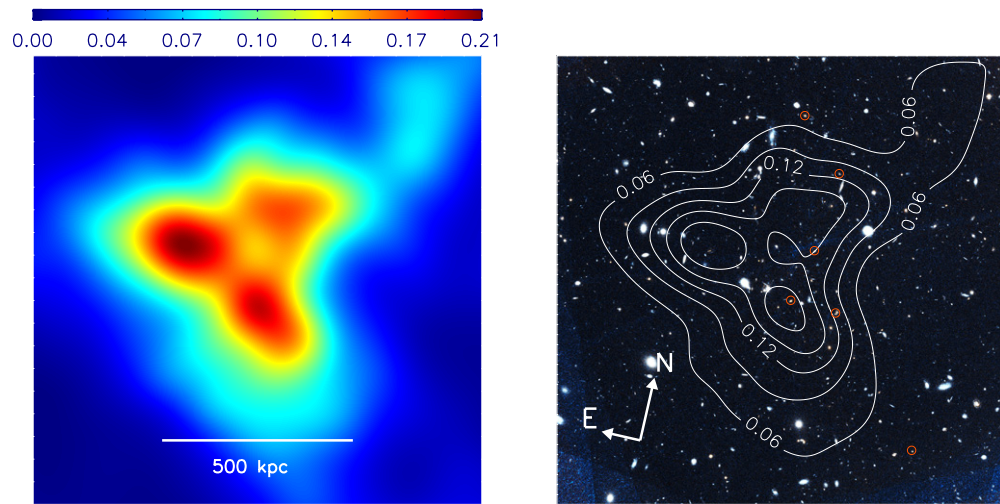(A color version of this figure is available in the online journal.)

Figure 8. Same as Figure 2 but for ISCS J1434+3427.
(A color version of this figure is available in the online journal.)

Figure 9. Same as Figure 2 but for ISCS J1432+3436.
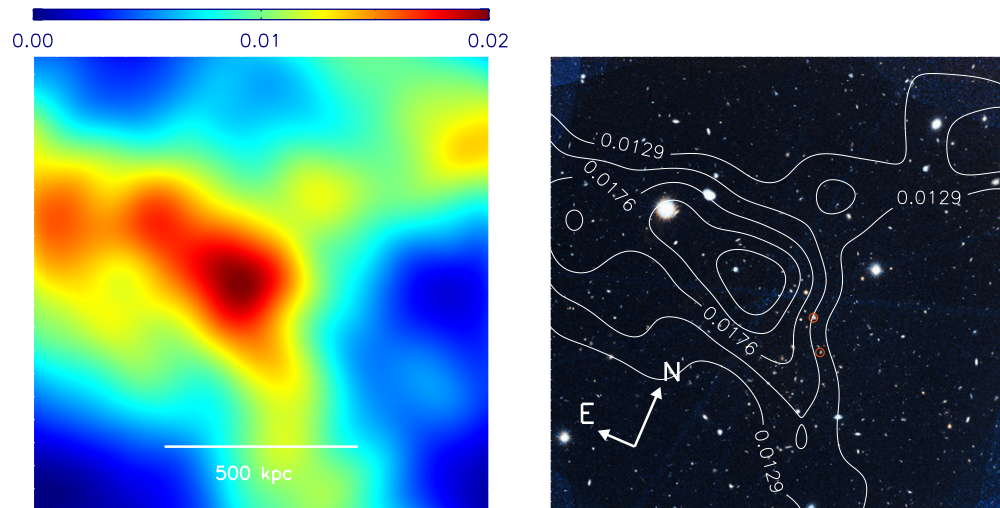(A color version of this figure is available in the online journal.)

Figure 10. Same as Figure 2 but for ISCS J1434+3519.
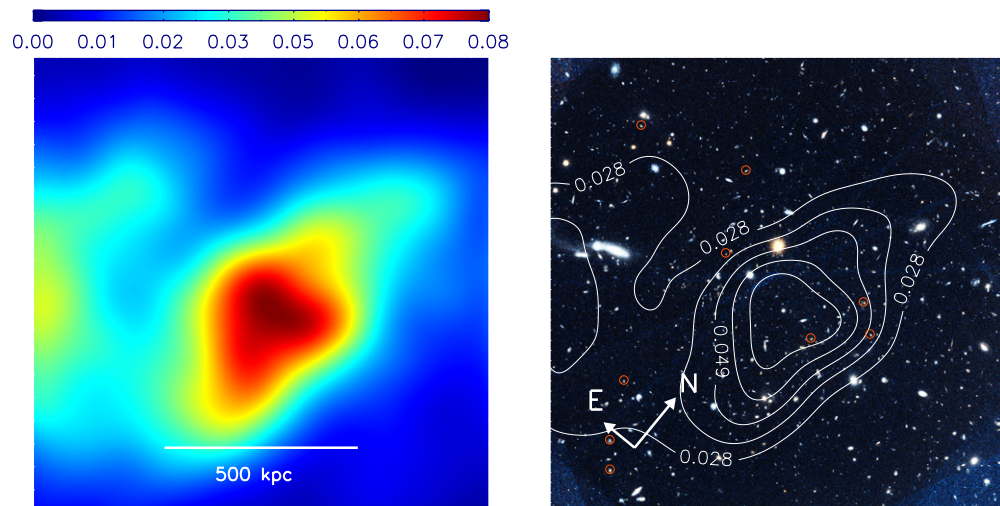(A color version of this figure is available in the online journal.)

Figure 11. Same as Figure 2 but for ISCS J1438+3414.
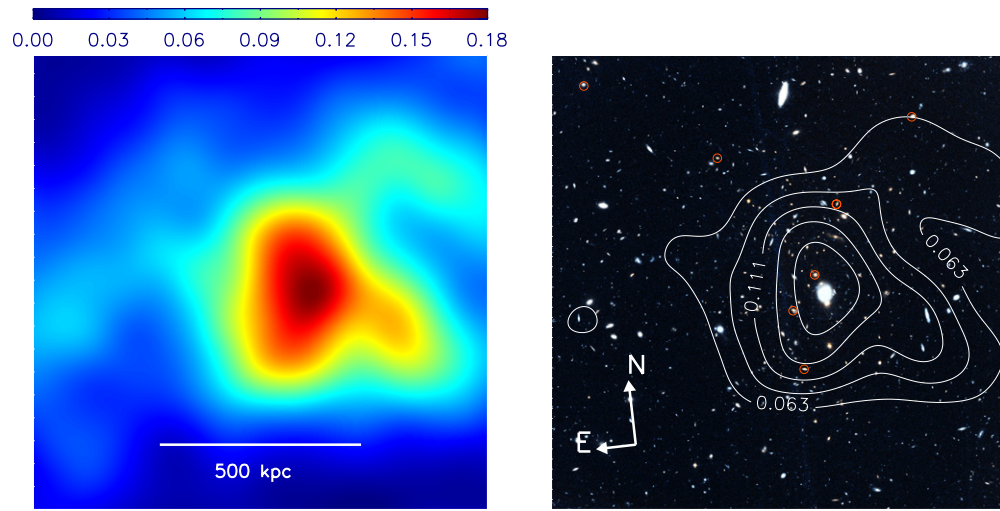(A color version of this figure is available in the online journal.)

Figure 12. Same as Figure 2 but for RCS 0220−0333.
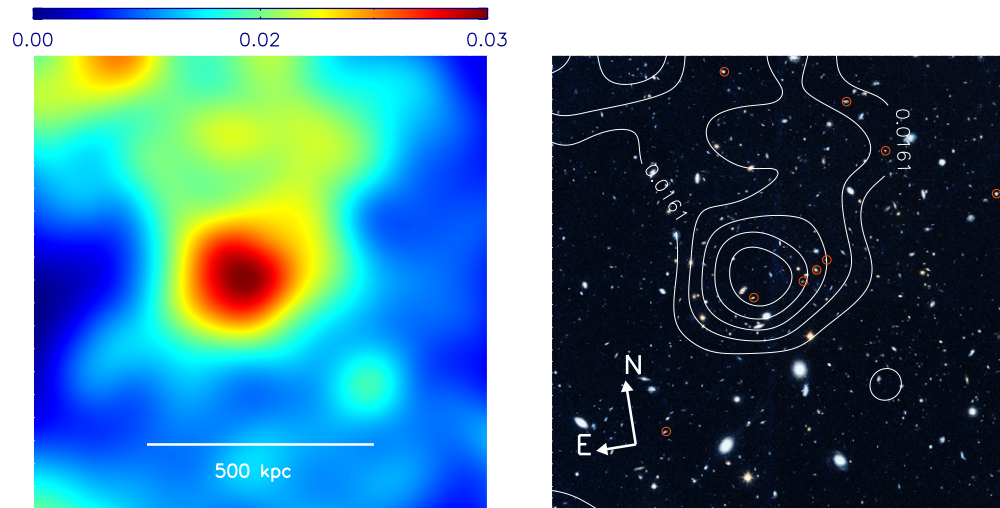(A color version of this figure is available in the online journal.)

Figure 13. Same as Figure 2 but for RCS 0221−0321.
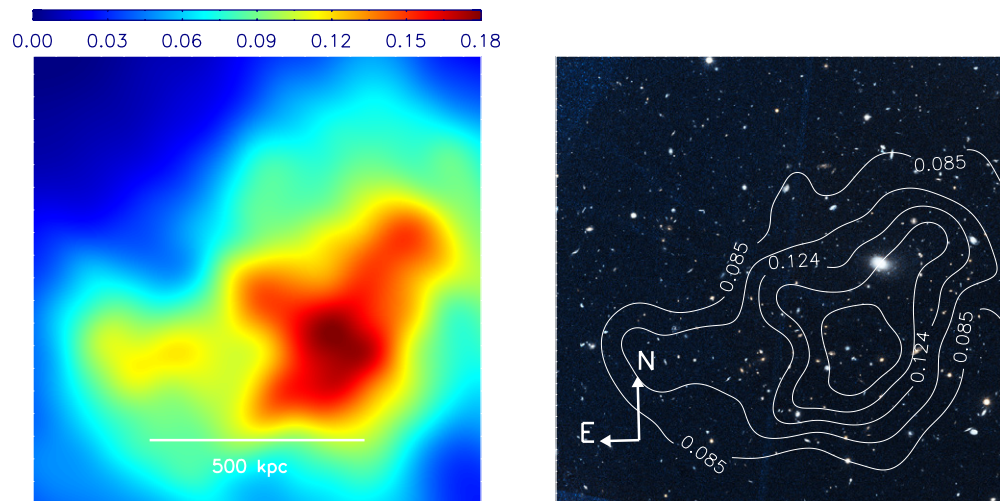(A color version of this figure is available in the online journal.)

Figure 14. Same as Figure 2 but for RCS 0337−2844.
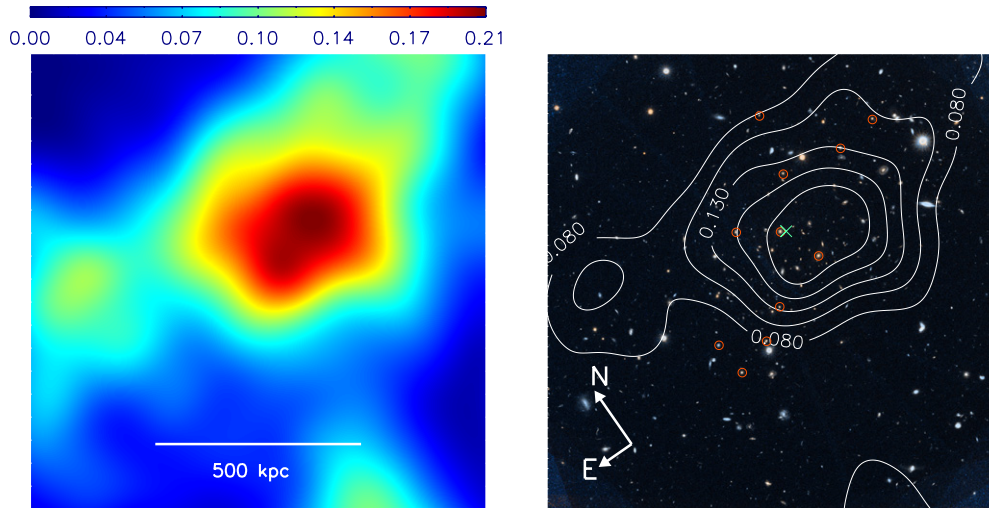(A color version of this figure is available in the online journal.)

Figure 15. Same as Figure 2 but for RCS 0439−2904.
(A color version of this figure is available in the online journal.)

3.3.2. XMMU J2205−0159 (z = 1.12)

XMMU2205−0159 was discovered in the *XMM-Newton* Distant Cluster Project (XDCP; Boehringer et al. 2006) survey in the archival image of QSO B2202-0209 at $z = 1.77$. The mass centroid is offset north of the brightest cluster galaxy (BCG) $(\alpha, \delta) \simeq (22{:}05{:}50.7, -01{:}59{:}30)$ by $\sim 17''$ (Figure 3). We derive a weak-lensing mass of $M_{200} = 3.0^{+1.6}_{-1.0} \times 10^{14}\, M_\odot$, making the cluster among the least massive clusters in our sample. Neither a dynamical nor an X-ray study of the cluster has been published to date.

3.3.3. XMMU J1229+0151 (z = 0.98)

XMMU J1229+0151 was serendipitously detected in the field targeted for the well-known quasar 3C 273. The cluster is hot and X-ray luminous with $T_X = 6.4^{+0.7}_{-0.6}$ keV and $L_X = 3 \times 10^{44}$ erg s^{-1} (Santos et al. 2009). Our lensing analysis predicts a velocity dispersion of 867^{+64}_{-69} km s^{-1} and gives a virial mass of $M_{200} = 5.3^{+1.7}_{-1.2} \times 10^{14}\, M_\odot$. This lensing mass agrees nicely with the X-ray mass $M_{200} = 5.7^{+1.0}_{-0.8} \times 10^{14}\, M_\odot$ when an isothermal β model with $\beta = 0.7$ and $r_c = 250$ kpc is assumed; no measurement of the X-ray surface brightness has been reported yet. However, the velocity dispersion 683 ± 62 km s^{-1} derived from 27 spectroscopic members (Santos et al. 2009) is significantly lower than the lensing prediction of 867^{+64}_{-69} km s^{-1}. Our convergence map shows a strong peak $\sim 10''$ northeast of the X-ray peak and the cluster galaxies (Figure 4).

3.3.4. WARPS J1415+3612 (z = 1.03)

The cluster WARPS J1415+3612 was discovered (Perlman et al. 2002) in the first phase of the Wide Angle *ROSAT* Pointed Survey (WARPS). The ICM temperature of the cluster has been measured from the *Chandra* (5.59 ± 0.84 keV; Allen et al. 2008) and *XMM-Newton* ($5.7^{+1.2}_{-0.7}$ keV; Maughan et al. 2006) data analysis. The cluster has been considered relaxed because of its symmetric X-ray emission (Maughan et al. 2006; Allen et al. 2008). Our weak-lensing mass map of the cluster also does not show any significant substructure, adding an additional support to the hypothesis. Both virial masses derived from X-ray

and lensing ($M_{200} = 4.6^{+1.5}_{-0.8} \times 10^{14}\, M_\odot$ and $4.7^{+2.0}_{-1.4} \times 10^{14}\, M_\odot$, respectively) are in excellent agreement.

The ACS image of the cluster shows a strongly lensed arc at $z = 3.898$. The source is a Lyα emitter and is located $\sim 7''$ away from the BCG (Huang et al. 2009). When we adopt this distance as the Einstein radius at $z = 3.898$, the value is consistent with the weak-lensing prediction $\theta_E(z = 3.898) = 8'' \pm 2''$ derived from the NFW fitting result; note also that the location of the weak-lensing mass peak is in good agreement with that of the BCG (Figure 5).

3.3.5. ISCS J1432+3332 (z = 1.11)

The ISCS J1432+3332 cluster was reported by Elston et al. (2006) as one of the first spectroscopically confirmed $z > 1$ clusters detected through the joint use of the FLAMINGOS Extragalactic Survey (FLAMEX; Elston et al. 2006), the NOAO Deep Wide-Field Survey (NDWFS; Brown et al. 2003), and the *Spitzer* IRAC Shallow Survey (ISCS; Eisenhardt et al. 2004) data sets. They estimated from eight spectroscopic members that the velocity dispersion of the cluster is 920 ± 230 km s^{-1}. Eisenhardt et al. (2008) reported a refined measurement of $\sigma_v = 734$ km s^{-1} using 23 redshifts; the authors did not quote an uncertainty and we estimate $\delta\sigma_v \sim 115$ km s^{-1}. The virial mass is estimated to be $M_{200} = 4.9^{+1.6}_{-1.2} \times 10^{14}\, M_\odot$. The mass contours are well traced by the cluster galaxies (Figure 6).

3.3.6. ISCS J1429+3437 (z = 1.26)

ISCS J1429+3437 was identified photometrically with the combined use of the ISCS and NDWFS data sets (Eisenhardt et al. 2008). From the nine spectroscopic members of Eisenhardt et al. (2008), we calculate the velocity dispersion to be 767 ± 295 km s^{-1}, which agrees well with the predicted velocity dispersion 732^{+70}_{-78} km s^{-1}. For the virial mass, we obtain $M_{200} = 5.4^{+2.4}_{-1.6} \times 10^{14}\, M_\odot$.

We detect two mass clumps within the ACS field of the cluster observation (Figure 7). The western mass peak is much stronger and spatially correlated with the cluster galaxy candidates. The much weaker eastern clump does not have any compact galaxy distribution. Nevertheless, the global east–west elongation of the mass distribution seems to follow the early-type galaxies
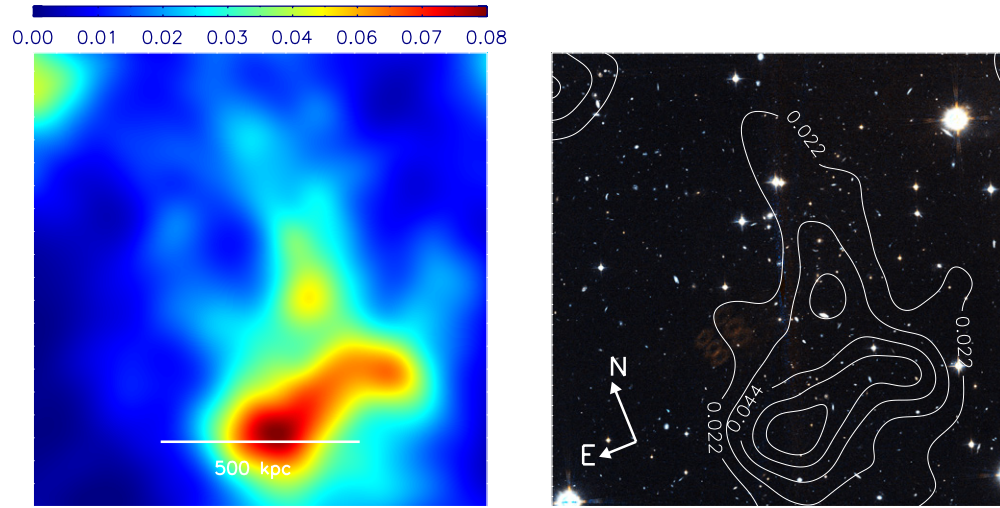
Figure 16. Same as Figure 2 but for RCS 2156−0448.
(A color version of this figure is available in the online journal.)
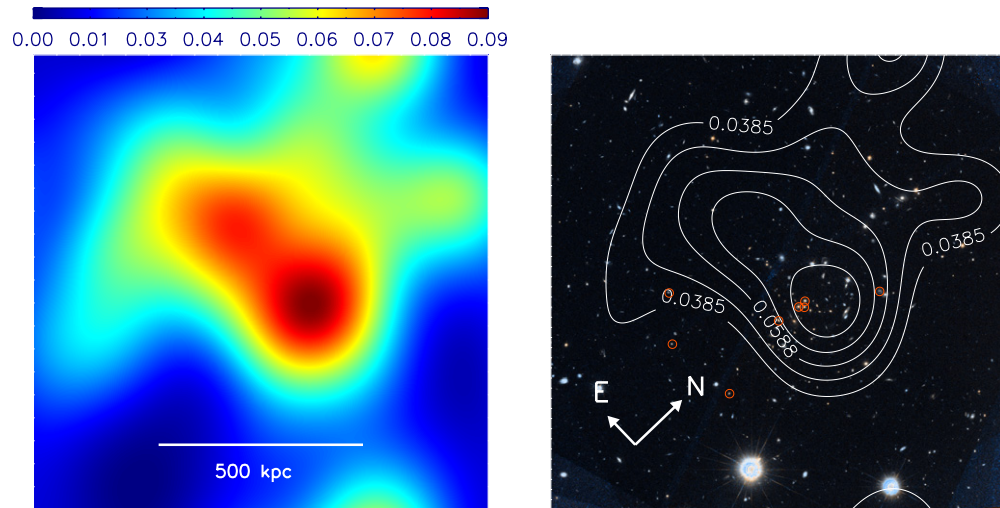

Figure 17. Same as Figure 2 but for RCS 1511+0903.
(A color version of this figure is available in the online journal.)

Figure 18. Same as Figure 2 but for RCS 2345−3632.
(A color version of this figure is available in the online journal.)

Figure 19. Same as Figure 2 but for RCS 2319+0038.
(A color version of this figure is available in the online journal.)

Figure 20. Same as Figure 2 but for XLSS J0223−0436.
(A color version of this figure is available in the online journal.)

Figure 21. Same as Figure 2 but for RDCS J0849+4452.
(A color version of this figure is available in the online journal.)

Figure 22. Same as Figure 2 but for RDCS J0910+5422.
(A color version of this figure is available in the online journal.)

Figure 23. Same as Figure 2 but for RDCS J1252−2927.
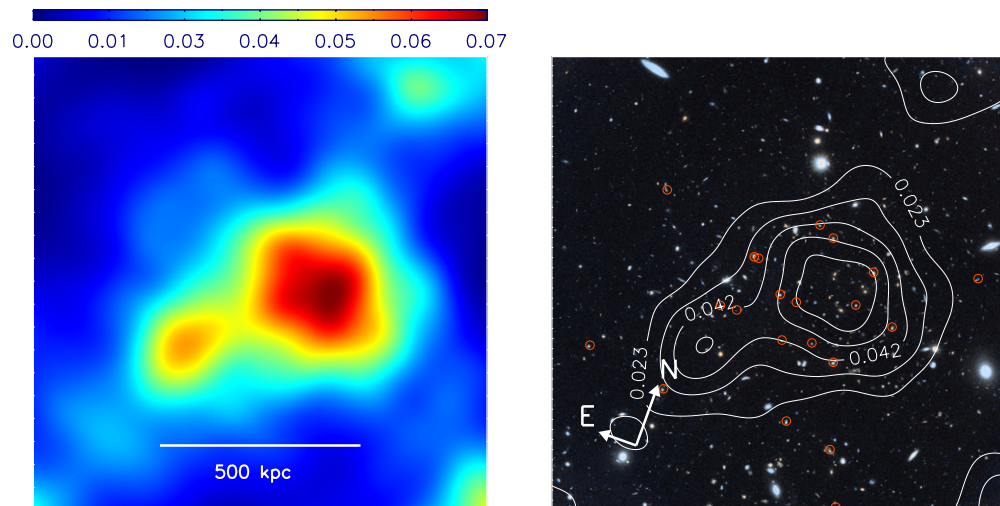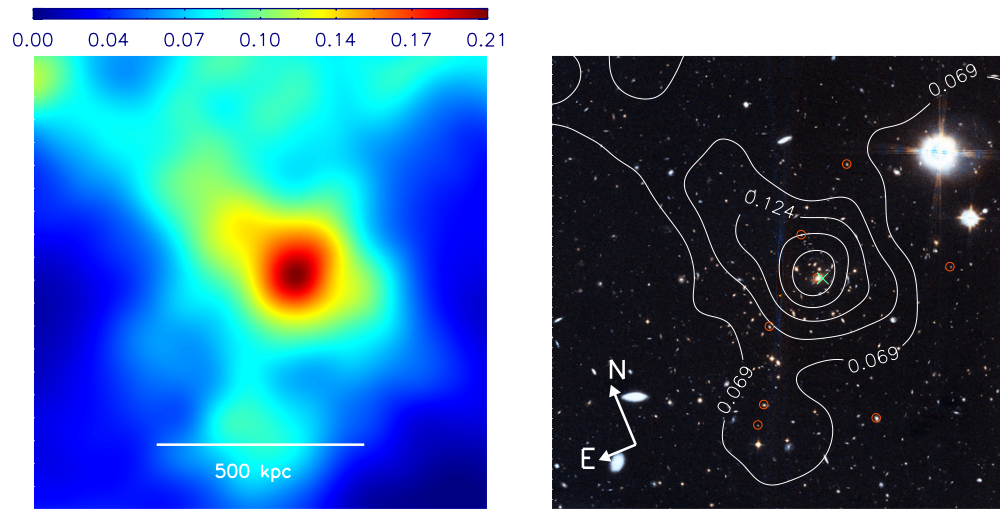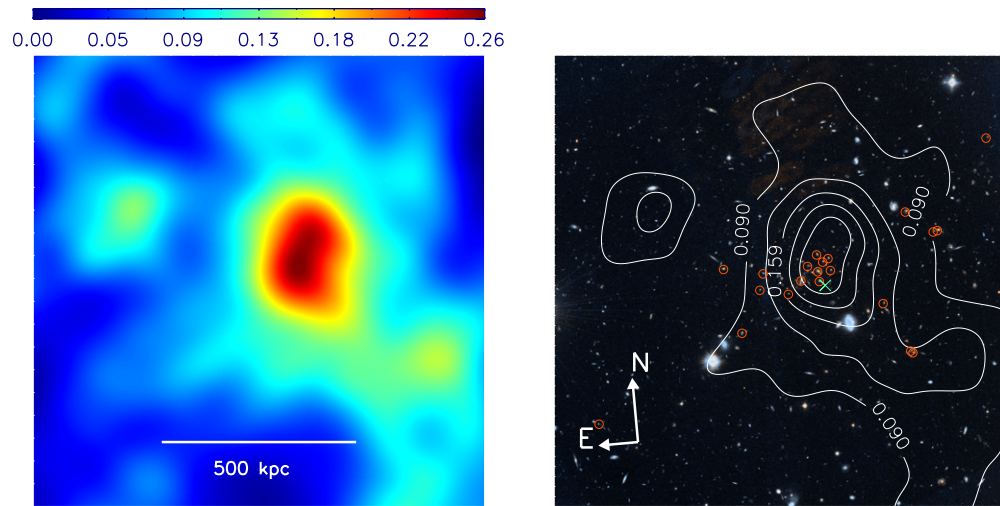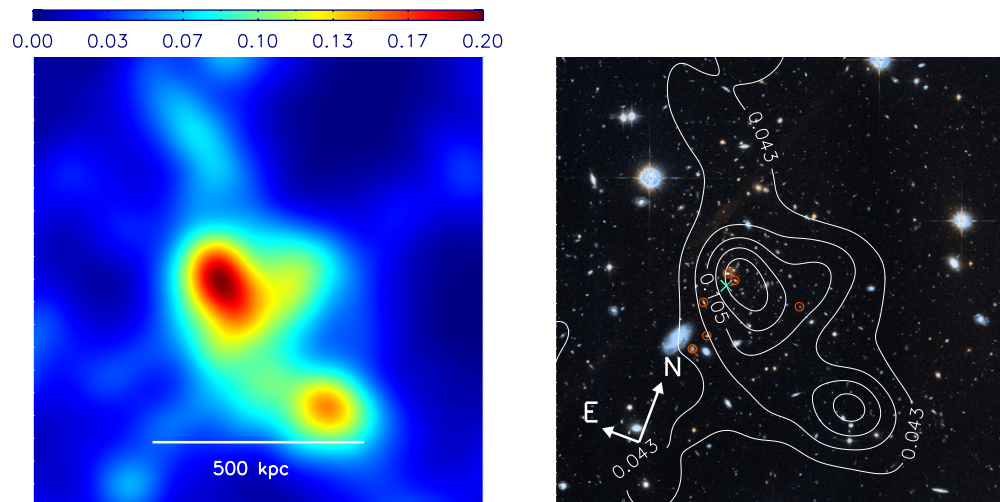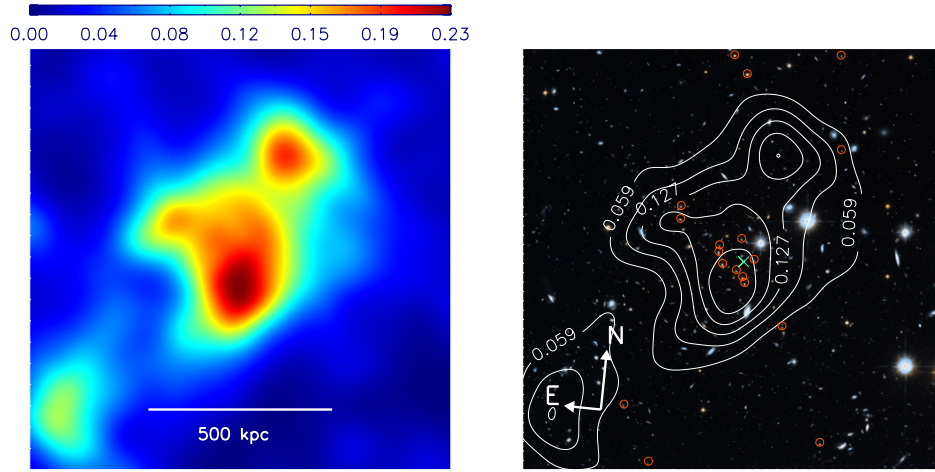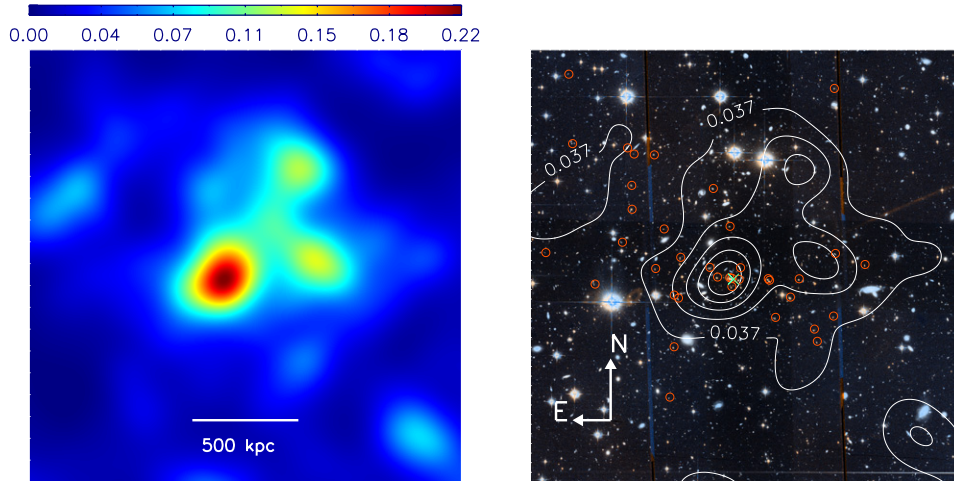(A color version of this figure is available in the online journal.)

in the field whose colors are consistent with that of the red sequence at the redshift of the cluster.

3.3.7. ISCS J1434+3427 (z = 1.24)

The ISCS J1434+3427 cluster, discovered in the ISCS and NDWFS survey, is reported to possess a pronounced filamentary structure (Brodwin et al. 2006). Although our mass reconstruction reveals a significant mass peak 10″ east of the compact galaxy distribution, the current i_{775} image is not deep enough ($\sim$2685 s) to study the substructure of this high-redshift cluster in detail. Because the cluster is located near the edge of the ACS field, we need to assume an azimuthal symmetry at large radius to obtain a mass estimate. This may substantially bias our measurement if the cluster departs significantly from the assumed axisymmetry. Nevertheless, we note that the predicted velocity dispersion of 770^{+113}_{-133} km s^{-1} from our lensing analysis is consistent with the dynamical velocity dispersion 863 ± 170 km s^{-1} that is derived from 11 cluster members (Meyers et al. 2011).

3.3.8. ISCS J1432+3436 (z = 1.35)

The cluster was discovered in the ISCS and NDWFS survey, and about eight members have been spectroscopically confirmed

(Eisenhardt et al. 2008). The cluster detection is very strong in our mass reconstruction despite both the high redshift and the shallowness (2235 s) of the i_{755} image. We estimate the virial mass to be $M_{200} = 5.3^{+2.6}_{-1.7} \times 10^{14}\,M_{\odot}$. The velocity dispersion derived from eight members is 807 ± 340 km s^{-1}, which agrees well with the lensing prediction of 912^{+92}_{-102} km s^{-1}.

3.3.9. ISCS J1434+3519 (z = 1.37)

Eisenhardt et al. (2008) report that five members have been spectroscopically confirmed. Our two-dimensional mass reconstruction (Figure 10) reveals a weak detection of a convergence peak near the cluster center defined by Eisenhardt et al. (2008) using photometric redshifts. The 15″ offset may be attributed to statistical noise because of the high-redshift, the low-mass, and the insufficient depth (1920 s) of the i_{775} image. The virial mass is determined to be $M_{200} = 2.8^{+2.9}_{-1.4} \times 10^{14}\,M_{\odot}$.

3.3.10. ISCS J1438+3414 (z = 1.41)

The discovery of ISCS J1438+3414 is reported by Stanford et al. (2005), who confirmed five spectroscopic members. Brodwin et al. (2011) quote a dynamical velocity dispersion of 757^{+247}_{-203} km s^{-1} from a total of 11 cluster members, which

Table 2
Cluster Properties

Cluster Name	z	σ_{vel} (km s^{-1})	σ_{vel}^{len} (km s^{-1})	T (keV)	M_{200}^{X} ($10^{14} M_\odot$)	c_{200}	r_{200} (Mpc)	M_{200}^{L} ($10^{14} M_\odot$)
XMMXCS J2215−1738	1.46	720 ± 110[a]	942^{+111}_{-126}	$4.1^{+0.6}_{-0.9}$ [1]	$2.0^{+0.5}_{-0.6}$	2.45 ± 0.11	$0.90^{+0.17}_{-0.14}$	$4.3^{+3.0}_{-1.7}$
XMMU J2205−0159	1.12		679^{+71}_{-79}			2.72 ± 0.10	$0.90^{+0.14}_{-0.12}$	$3.0^{+1.6}_{-1.0}$
XMMU J1229+0151	0.98	683 ± 62[b]	867^{+64}_{-69}	$6.4^{+0.7}_{-0.6}$ [2]	$5.7^{+1.0}_{-0.8}$	2.67 ± 0.06	$1.12^{+0.11}_{-0.10}$	$5.3^{+1.7}_{-1.2}$
WARPS J1415+3612	1.03	807 ± 185[c]	893^{+73}_{-80}	$5.7^{+1.2}_{-0.7}$ [3]	$4.6^{+1.5}_{-0.8}$	2.66 ± 0.08	$1.09^{+0.14}_{-0.12}$	$4.7^{+2.0}_{-1.4}$
ISCS J1432+3332	1.11	734 ± 115[d]	834^{+64}_{-70}			2.61 ± 0.06	$1.06^{+0.11}_{-0.09}$	$4.9^{+1.6}_{-1.2}$
ISCS J1429+3437	1.26	767 ± 295[e]	732^{+70}_{-78}			2.51 ± 0.08	$1.04^{+0.13}_{-0.12}$	$5.4^{+2.4}_{-1.6}$
ISCS J1434+3427	1.24	863 ± 170[e]	770^{+113}_{-133}			2.68 ± 0.14	$0.82^{+0.19}_{-0.14}$	$2.5^{+2.2}_{-1.1}$
ISCS J1432+3436	1.35	807 ± 340[e]	912^{+92}_{-102}			2.46 ± 0.08	$1.00^{+0.14}_{-0.12}$	$5.3^{+2.6}_{-1.7}$
ISCS J1434+3519	1.37		812^{+137}_{-166}			2.59 ± 0.15	$0.81^{+0.21}_{-0.16}$	$2.8^{+2.9}_{-1.4}$
ISCS J1438+3414	1.41	757^{+247}_{-208} [f]	833^{+127}_{-150}	$4.9^{+3.4}_{-1.6}$ [4]	$3.2^{+3.9}_{-1.4}$	2.55 ± 0.13	$0.82^{+0.18}_{-0.14}$	$3.1^{+2.6}_{-1.4}$
RCS 0220−0333	1.03		881^{+68}_{-74}			2.66 ± 0.07	$1.09^{+0.12}_{-0.11}$	$4.8^{+1.8}_{-1.3}$
RCS 0221−0321	1.02	710 ± 150[g]	699^{+83}_{-94}			2.90 ± 0.13	$0.80^{+0.16}_{-0.13}$	$1.8^{+1.3}_{-0.7}$
RCS 0337−2844	1.1		863^{+100}_{-113}			2.61 ± 0.10	$1.08^{+0.17}_{-0.15}$	$4.9^{+2.8}_{-1.7}$
RCS 0439−2904	0.95	1080 ± 320[h]	831^{+68}_{-74}	$1.5^{+1.0}_{-0.4}$ [5]	$0.46^{+6.0}_{-1.7}$	2.73 ± 0.08	$1.09^{+0.13}_{-0.11}$	$4.3^{+1.7}_{-1.2}$
RCS 2156−0448	1.07		691^{+137}_{-172}			2.86 ± 0.20	$0.78^{+0.26}_{-0.18}$	$1.8^{+2.5}_{-1.0}$
RCS 1511+0903	0.97	717 ± 208[e]	699^{+94}_{-109}			2.92 ± 0.13	$0.82^{+0.17}_{-0.14}$	$1.9^{+1.4}_{-0.8}$
RCS 2345−3632	1.04	670 ± 190[i]	684^{+71}_{-79}			2.81 ± 0.09	$0.87^{+0.11}_{-0.10}$	$2.4^{+1.1}_{-0.7}$
RCS 2319+0038	0.91	990 ± 240[j]	898^{+67}_{-71}	$6.2^{+0.9}_{-0.8}$ [6]	$5.4^{+1.2}_{-1.0}$	2.70 ± 0.08	$1.22^{+0.15}_{-0.13}$	$5.8^{+2.3}_{-1.6}$
XLSS J0223−0436	1.22	799 ± 129[e]	1011^{+73}_{-79}	$3.8^{\cdots}_{-1.9}$ [7]	$2.4^{\cdots}_{-1.5}$	2.46 ± 0.06	$1.18^{+0.12}_{-0.11}$	$7.4^{+2.5}_{-1.8}$
RDCS J0849+4452	1.26	720 ± 140[k]	740^{+41}_{-44}	5.2 ± 1.3 [8]	$3.8^{+1.5}_{-1.4}$	2.55 ± 0.05	$0.98^{+0.77}_{-0.07}$	$4.4^{+1.1}_{-0.9}$
RDCS J0910+5422	1.11	675 ± 190[l]	895^{+48}_{-51}	6.4 ± 1.4 [8]	$7.4^{+2.6}_{-2.3}$	2.61 ± 0.05	$1.07^{+0.08}_{-0.07}$	$5.0^{+1.2}_{-1.0}$
RDCS J1252−2927	1.24	747^{+74}_{-84} [m]	957^{+45}_{-48}	7.6 ± 1.2 [8]	$4.4^{+1.1}_{-1.0}$	2.47 ± 0.03	$1.14^{+0.06}_{-0.06}$	$6.8^{+1.2}_{-1.0}$
XMMU J2235−2557	1.39	802^{+77}_{-48} [n]	1145 ± 70	$8.6^{+1.3}_{-1.2}$ [9]	$6.1^{+1.4}_{-1.2}$	2.38 ± 0.04	$1.13^{+0.08}_{-0.07}$	$7.3^{+1.7}_{-1.4}$
CL J1226+3332	0.89	1143 ± 162[o]	1237 ± 22	10.4 ± 0.6 [10]	$12.2^{+1.1}_{-1.0}$	2.52 ± 0.03	$1.68^{+0.10}_{-0.09}$	$13.7^{+2.4}_{-2.0}$
MS 1054−0321	0.83	1156 ± 82[p]	1150 ± 50	$8.9^{+1.0}_{-0.8}$ [11]	$12.8^{+2.2}_{-1.7}$	2.61 ± 0.03	$1.59^{+0.11}_{-0.09}$	$10.8^{+2.1}_{-1.8}$
CL J0152−1357	0.84	919 ± 168[q]	903 ± 56	6.7 ± 1.0 [8]	$7.3^{+1.8}_{-1.7}$	2.81 ± 0.04	$1.17^{+0.09}_{-0.06}$	$4.4^{+0.7}_{-0.5}$
RDCS J0848+4453	1.27	700 ± 180[k]	762 ± 120	3.8 ± 1.9 [8]	$1.1^{+0.9}_{-0.7}$	2.57 ± 0.05	$0.96^{+0.09}_{-0.07}$	$3.1^{+1.0}_{-0.8}$

References. [a] Hilton et al. 2010; [b] Santos et al. 2009; [c] Huang et al. 2009; [d] Eisenhardt et al. 2008; [e] Meyers et al. 2011; [f] Brodwin et al. 2011; [g] Andreon et al. 2008; [h] Cain et al. 2008; [i] D. G. Gilbank et al. 2011, in preparation; [j] Gilbank et al. 2008; [k] Jee et al. 2006; [l] Mei et al. 2006; [m] Demarco et al. 2007; [n] Rosati et al. 2009; [o] Holden et al. 2009; [p] Tran et al. 2007; [q] Demarco et al. 2005; [1] Hilton et al. 2010; [2] Santos et al. 2009; [3] Maughan et al. 2006; [4] Andreon et al. 2011; [5] Cain et al. 2008; [6] Hicks et al. 2008; [7] Bremer et al. 2006; [8] Ettori et al. 2009; [9] Rosati et al. 2009; [10] Maughan et al. 2007; [11] Jee et al. 2005b.

can be converted to $M_{200} = 2.3^{+2.4}_{-2.1} \times 10^{14} M_\odot$ using the mass–dispersion relation from Evrard et al. (2008). These values are consistent with those from our lensing analysis, which give 833^{+127}_{-150} km s^{-1} and a virial mass of $M_{200} = 3.1^{+2.6}_{-1.4} \times 10^{14} M_\odot$. Andreon et al. (2011) measured an X-ray temperature $T_X = 4.9^{+3.4}_{-1.6}$ keV from the relatively deep ($\sim$150 ks) *Chandra* data of the cluster. This temperature is consistent with the measurement ($3.3^{+1.9}_{-1.0}$ keV) of Brodwin et al. (2011) obtained from the same data. Assuming $\beta = 0.7$ and $rc \sim 100$ kpc, we convert $T_X = 4.9^{+3.4}_{-1.6}$ keV to $M_{200}^{X} = 3.2^{+3.8}_{-1.4} M_\odot$, which also agrees well with our lensing mass. The centroid of the diffuse X-ray emission is in good spatial agreement with that of the weak-lensing mass.

3.3.11. RCS 0220−0333 (z = 1.03)

The clusters with a prefix RCS hereafter were mostly discovered in the Red-sequence Cluster Survey-I (Gladders & Yee 2005); the exception is RCS 1511+0903, which was discovered in the Red-sequence Cluster Survey-II (Gilbank et al. 2011). RCS 0220−0333 is an optically rich cluster at $z = 1.03$. In the ACS pseudo-color composite image, the early-type galaxies with $i_{775} - z_{850} \sim 0.9$ appear to form a north–south filamen-

tary structure. The cluster is strongly detected in lensing. The mass centroid lies close to the cluster member with pronounced strong-lensing features. However, the mass distribution does not indicate the north–south elongation seen in the cluster galaxies. We obtain a virial mass of $M_{200} = 4.8^{+1.8}_{-1.3} \times 10^{14} M_\odot$ with a predicted velocity dispersion of 881^{+68}_{-74} km s^{-1}.

3.3.12. RCS 0221−0321 (z = 1.02)

This optically rich galaxy cluster RCS 0221−0321 is clearly visible in our mass reconstruction. The mass map shows a significant mass clump aligned with the optical center (e.g., see the isodensity contours for red galaxies from Andreon et al. 2008). However, this cluster is found to be one of the least massive clusters in our sample. We estimate the virial mass to be $M_{200} = 1.8^{+1.3}_{-0.7} \times 10^{14} M_\odot$. The predicted velocity dispersion of 699^{+83}_{-94} km s^{-1} agrees well with the dynamical measurement 710 ± 150 km s^{-1} based on 21 spectroscopic members (Andreon et al. 2008).

3.3.13. RCS 0337−2844 (z = 1.10)

RCS 0337−2844 is clearly visible in our two-dimensional mass map, which shows a good mass–galaxy correlation. The

exposure time of the i_{755} image of this cluster is the shortest among the clusters studied here, which indicates that this strong weak-lensing signal is due to a significant mass. We estimate $M_{200} = 4.9^{+2.8}_{-1.7} \times 10^{14} \, M_{\odot}$. No spectroscopic data have been published to date.

3.3.14. RCS 0439−2904 (z = 0.95)

Barrientos et al. (2004) reported that RCS 0439−2904 is an optically rich cluster ($\sim 9\sigma$ in the K_s image) at a high redshift. Cain et al. (2008) measured the X-ray temperature of the cluster from the 200 ks *Chandra* to be $T_x = 1.5^{+1.0}_{-0.4}$ keV, which is significantly lower than what the optical richness suggested. The single isothermal β model gives $M_{200} = 4.6^{+6.0}_{-1.7} \times 10^{13} \, M_{\odot}$. On the other hand, the mass–richness relation implies a much higher mass by at least an order of magnitude. Because their velocity histogram shows that there are multiple components, Cain et al. (2008) interpreted this large discrepancy as indicating the presence of two clusters along the line-of-sight direction. They also claim that the unexpectedly high gas fraction obtained when a single component is assumed supports the two-component interpretation.

The line-of-sight hypothesis makes our lensing study of the cluster interesting. If there is indeed a line-of-sight superposition of two clusters, the mass estimate from lensing should give the sum of the two clusters as opposed to the single-component X-ray model. Our analysis shows that the cluster virial mass is $M_{200} = 4.3^{+1.7}_{-1.2} \times 10^{14} \, M_{\odot}$, nearly a factor of 10 higher than the X-ray prediction as was also indicated by the mass–richness relation. Interestingly, our predicted velocity dispersion 831^{+68}_{-74} km s^{-1} is consistent with the dynamical measurement 1080 ± 320 km s^{-1} of Cain et al. (2008). The lensing mass is consistent with the mass–richness relation if the cluster is assumed to consist of two clusters; the new lensing mass shifts the Model II data point of Figure 3 of Cain et al. (2008) upward in such a way that the new point is well bracketed by the 1σ scatter of the mass–richness relation of Blindert (2006).

3.3.15. RCS 2156−0448 (z = 1.07)

The cluster RCS 2156−0448 was reported as an optically rich cluster with a strong-lensing arc candidate by Gladders et al. (2003). If confirmed, the presence of this arc suggests that the cluster is massive as indicated by its optical richness. However, Gladders et al. (2003) commented that this candidate should be considered the least likely among their secondary sample.

Our weak-lensing mass reconstruction reveals only a weak convergence peak near the arc candidate. Instead, the mass map shows a more significant mass peak $\sim 70''$ south of the assumed cluster center. Our visual inspection of the ACS image shows that on this location there seems to be also early-type galaxies whose colors are consistent with that of the cluster red sequence.

Nevertheless, one must be reminded that the combined ($i_{775} + z_{850}$) ACS image of the cluster is the shallowest among our 22 cluster samples, which gives the lowest number density of background galaxies (~ 50 arcmin^{-2}). Hence, the mass–galaxy comparison should await a future analysis with deeper images. Our mass presented here is estimated by placing the center on the strong-lensing candidate of Gladders et al. (2003).

3.3.16. RCS 1511+0903 (z = 0.97)

The ACS image of RCS 1511+0903 shows a compact distribution of early-type galaxies whose colors are consistent with the cluster redshift $z = 0.97$. The cluster is clearly visible in

our mass reconstruction, which reveals a strong mass peak at the location of the cluster galaxies. Based on nine redshifts, Meyers et al. (2011) estimate the velocity dispersion of the cluster to be 717 ± 208 km s^{-1}, which is consistent with our lensing prediction of 699^{+94}_{-109} km s^{-1}. The virial mass of the cluster from our lensing analysis is $M_{200} = 1.9^{+1.4}_{-0.8} \times 10^{14} \, M_{\odot}$.

3.3.17. RCS 2345−3632 (z = 1.04)

RCS 2345−3632 is an optically rich cluster at $z = 1.04$ with 23 spectroscopically confirmed cluster galaxies. The dynamical velocity dispersion of 670 ± 190 km s^{-1} is consistent with the lensing prediction of 684^{+71}_{-79} km s^{-1}. The two-dimensional mass map agrees well with the cluster galaxy distribution (Figure 18). The relatively deep ACS image allows us to utilize ~ 103 background galaxies per square arcmin, and thus the resulting mass reconstruction should be considered the most reliable among the eight RCS clusters presented in this paper. We estimate that the virial mass of the cluster is $M_{200} = 2.4^{+1.1}_{-0.7} \times 10^{14} \, M_{\odot}$.

3.3.18. RCS 2319+0038 (z = 0.91)

RCS 2319+0038 is a strong-lensing cluster showing at least two spectacular arcs (Gladders et al. 2003). The recent ACS images of the cluster reveal more strong-lensing features (at least seven tangential and two radial arc candidates). Gilbank et al. (2008) discovered that the cluster is in fact part of a supercluster containing two other clusters, RCS 2319+0030 and RCS 2320+0033. All three clusters are well detected in the *Chandra* X-ray observations with similar gas temperatures ~ 6 keV (Hicks et al. 2008). RCS 2319+0038 is separated from RCS 2320+0033 and RCS 2319+0030 by $\sim 5'$ and $\sim 7'$, respectively, and therefore our lensing analysis based on the ACS image covering the central $3' \times 3'$ region of RCS 2319+0038 is not likely to be affected by these two other structures. Gilbank et al. (2008) reported a velocity dispersion of 990 ± 240 km s^{-1}, which agrees well with the current lensing prediction of 898^{+67}_{-71} km s^{-1}. Our convergence map reveals a single strong mass peak at the center of the strong-lensing system without any significant substructures. Both this mass map and the tangential shear profile suggest that the cluster is relaxed. The virial mass derived from the X-ray measurements of Hicks et al. (2008; $T_X = 6.2^{+0.9}_{-0.8}$ keV, $r_c = 100$ kpc, and $\beta = 0.65$) is $M_{200} = 5.4^{+1.2}_{-1.0} \times 10^{14} \, M_{\odot}$, again in good agreement with the lensing result $M_{200} = 5.8^{+2.3}_{-1.6} \times 10^{14} \, M_{\odot}$.

3.3.19. XLSS 0223−0436 (z = 1.22)

XLSS 0223−0436 was discovered in the *XMM* LSS survey (Pierre et al. 2004; Andreon et al. 2005), and Bremer et al. (2006) presented detailed analysis of the X-ray and optical/near-IR data of the cluster. They estimated an X-ray temperature of 3.8 keV with a 1σ lower limit of 1.9 keV and an unconstrained upper limit. This X-ray temperature 3.8 keV is somewhat lower than what one predicts from the dynamical velocity dispersion 799 ± 129 km s^{-1} (based on 24 redshifts). Because Bremer et al. (2006) report that the existing *XMM-Newton* data do not constrain the upper limit of their temperature, this cluster is excluded in our investigation of the lensing-mass–temperature relation. Our lensing analysis predicts $\sigma_v = 1011^{+73}_{-79}$ km s^{-1}, which is even higher than the dynamical measurement. We estimate that the virial mass of the cluster is $M_{200} = 7.4^{+2.5}_{-1.8} \times 10^{14} \, M_{\odot}$.

Bremer et al. (2006) reported that the optical image of the cluster shows a compact distribution of >12 galaxies within

a 125 kpc radius centered on the X-ray peak. The location of our weak-lensing mass peak agrees well with the X-ray and the optical centers.

3.3.20. RDCS J0849+4452 (z = 1.26)

RDCS J0849+4452 was discovered in the *ROSAT* Deep Cluster Survey (RDCS; Rosati et al. 1998), and followup near-IR imaging showed an excess of red ($1.8 < J-K < 2.1$) galaxies around the peak of the X-ray emission. Cluster galaxies were spectroscopically confirmed using the Keck telescope (Rosati et al. 1999). Stanford et al. (2001) measured an X-ray temperature of $T_x = 5.8^{+2.8}_{-1.7}$ keV from the *Chandra* data analysis; based on newer calibration data, Ettori et al. (2009) reported $T_x = 5.2 \pm 1.3$ keV. The cluster was one of the ACS Guaranteed Time Observation (GTO) high-redshift cluster targets, and the color–magnitude relation and the weak-lensing analysis have been presented by Mei et al. (2006) and Jee et al. (2006), respectively. Jee et al. (2006) quoted a projected mass of $M_{\rm proj} = (2.1 \pm 0.7) \times 10^{14} M_{\odot}$ within a 0.5 Mpc aperture radius, which is consistent with the projected X-ray mass $\sim 2.3 \times 10^{14} M_{\odot}$, which was obtained from their re-analysis of the *Chandra* data. In the present paper, we perform a weak-lensing analysis using a slightly deeper set of the ACS images, the result of stacking both the GTO data (Prop. ID 9919) and the high-z supernova search data (Prop. ID 10496). The new mass is in good agreement with the Jee et al. (2006) result; in the present paper we quote a virial mass $M_{200} = 4.4^{+1.1}_{-0.9} \times 10^{14} M_{\odot}$ ($r_{200} = 0.98$) rather than a projected mass. The cluster shows a strong-lensing features around the BCG. The two-dimensional mass map (Figure 21) reveals two significant mass clumps. The stronger one coincides with the centers of the X-ray emission and the optical center while the weaker seems to be associated with a foreground group. Both clumps were also shown in the mass reconstruction of Jee et al. (2006).

3.3.21. RDCS J0910+5422 (z = 1.11)

Discovered in the RDCS, the cluster was confirmed with near-IR and spectroscopic observations by Stanford et al. (2002). Ettori et al. (2009) measured an X-ray temperature of 6.4 ± 1.4 keV from 200 ks *Chandra* data, slightly lower than the measurement ($7.2^{+2.2}_{-1.4}$ keV) by Stanford et al. (2002). Combining 6.4 ± 1.4 keV with $r_c = 147$ kpc and $\beta = 0.843$, we obtain $M_{200} = 7.7^{+3.2}_{-2.2} \times 10^{14} M_{\odot}$ assuming an isothermal β profile. Our weak-lensing analysis yields a cluster mass $M_{200} = 5.0^{+1.2}_{-1.0} \times 10^{14} M_{\odot}$ ($r_{200} = 1.07$ Mpc), slightly lower than, but statistically consistent with, this X-ray result. The velocity dispersion estimated from 25 redshifts by Mei et al. (2006) is 675 ± 190 km s^{-1}, lower than our lensing prediction of 895^{+48}_{-51} km s^{-1} and the X-ray mass. Our mass reconstruction reveals two significant peaks. The stronger one is in good spatial agreement with the optical and X-ray centers whereas no apparent red sequence is found at the location of the secondary peak.

3.3.22. RDCS J1252−2927 (z = 1.24)

RDCS J1252−2927 was confirmed as a cluster at $z = 1.24$ based on an extensive spectroscopic campaign using the Very Large Telescope (Lidman et al. 2004). Rosati et al. (2004) presented the first X-ray analysis of the cluster based on both deep *Chandra* and *XMM-Newton* observations, which gives an X-ray temperature of $T_X = 6.0^{+0.7}_{-0.5}$ keV. A revised temperature of $T_X = 6.5 \pm 0.5$ keV is reported in Lombardi et al. (2005)

after the application of the new calibration of the *Chandra* instrument. The most recent analysis by Ettori et al. (2009) gives $T_X = 7.6 \pm 1.2$ keV.

Assuming the structural parameters $r_c = 79$ kpc and $\beta = 0.53$, we translate the temperature $T_x = 7.6 \pm 1.2$ keV into a virial mass $M_{200} = (4.4 \pm 1.0) \times 10^{14} M_{\odot}$ or a projected mass at $r = 1$ Mpc of $M_{\rm proj} = (7.1 \pm 1.1) \times 10^{14} M_{\odot}$. Using ACS data, Lombardi et al. (2005) quote a projected weak-lensing mass of $M(<1{\rm Mpc}) = (8.0 \pm 1.3) \times 10^{14} M_{\odot}$, which is higher than the X-ray result by $\sim 1\sigma$. Our lensing analysis based on deeper ACS images gives a virial mass of $M_{200} = 6.8^{+1.2}_{-1.0} \times 10^{14} M_{\odot}$ or a projected mass of $M(<1{\rm Mpc}) = (8.4 \pm 1.2) \times 10^{14} M_{\odot}$, which is consistent with the result of Lombardi et al. (2005). The current lensing analysis predicts $\sigma_v = 957^{+45}_{-48}$ km s^{-1}, higher than the dynamical measurement $\sigma_v = 747^{+74}_{-84}$ km s^{-1} that Demarco et al. (2007) obtained from 38 redshifts. Lombardi et al. (2005) discussed the possibility of a systematic overestimation of the mass in lensing because of a line-of-sight contamination. Demarco et al. (2007) reported that there is a possible group centered at $z = 0.74$ composed of 33 members in the range $0.70 < z < 0.79$. The projected distribution, however, is not compact, but is mostly scattered across the field. In addition, the deep (~ 190 ks) *Chandra* data do not hint at the presence of any significant intervening structure.

Our mass reconstruction reveals three significant mass peaks. The strongest one coincides with the optical and the X-ray centers. The other two weaker clumps do not correlate well with the red sequence of the cluster nor the group at $z = 0.74$. We note that these two mass clumps are also clearly seen in Figure 9 of Lombardi et al. (2005).

4. COMPARISON WITH OTHER CLUSTER PROPERTIES

The weak-lensing masses presented in the present work are used to study mass versus observable relations in the high-redshift universe. A comparable study but for a lower redshift sample was carried out by Hoekstra (2007) for 20 X-ray luminous clusters. Our study enables us to examine if the mass versus mass-observable relation holds across a wide range of redshifts.

As many clusters in our sample are the results of relatively recent discoveries, a large fraction of them still lack information on their velocity dispersion and X-ray properties. In subsequent analysis, we enlarge the current sample by adding five more high-redshift clusters in our previous lensing studies: XMMU J2235.3−2557 $z = 1.4$ (Jee et al. 2009), CL J1226+3332 $z = 0.89$ (Jee & Tyson 2009), CL J0152−1357 $z = 0.84$ (Jee et al. 2005a), MS 1054−0321 $z = 0.83$ (Jee et al. 2005b), and RX J0848+4453 $z = 1.27$ (Jee et al. 2006). We refer readers to the individual papers for detailed information on each cluster.

In order to avoid any potential scatter introduced by variations in the mass determination method, we re-calculated the NFW parameters for these additional clusters using the same mass–concentration relation employed in the present paper.

4.1. Dynamical Velocity Dispersion

Table 2 lists the dynamical velocity dispersions and the predicted values from the lensing analysis for the combined sample. There are a total of 23 clusters whose velocity dispersions are available either in the literature or through our collaborations (Meyers et al. 2011; D. G. Gilbank et al. 2011, in preparation).
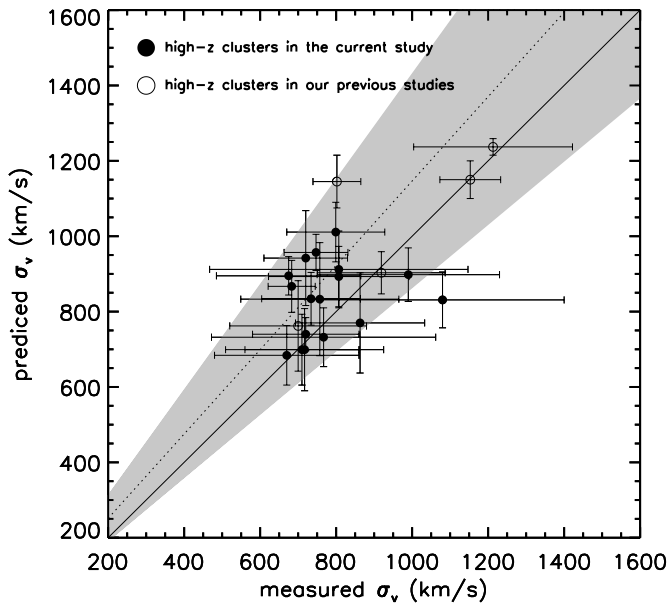
Figure 24. Dynamical velocity dispersion vs. lensing prediction. We use filled circles to represent the results for the clusters studied here. Open circles show the results for the high-z clusters in our previous publications. The solid line represents the line of equality The linear fit to the result is shown with the dotted line while the 1σ range of the slope is depicted by the gray region.

Figure 24 shows the comparison of the lensing prediction from the SIS fit with the dynamical measurement for these 23 clusters. The filled and open circles represent the clusters analyzed in the present paper and in our previous studies, respectively. The dotted line is a fit to the data, whose slope $\alpha = 1.12 \pm 0.31$ and intercept $b = 28 \pm 260$ km s^{-1} are consistent with the line of equality (solid); the shadow represents the 1σ range of the slope. Individual data points have rather large scatters around these lines mostly due to their large statistical (e.g., small number of known spectroscopic members and source galaxies) and systematic (e.g., cluster mass profile being different from SIS) uncertainties.

4.2. X-Ray Properties

Scaling relations between X-ray properties and lensing masses not only provide invaluable insight into the physical mechanism of cluster formation, but also help us to calibrate mass estimates based on X-ray data. For a virialized cluster, we expect the mass to scale with the gas temperature via the power-law relation $M \propto T^{3/2}$ (Kaiser 1986). In this paper, we use the following specific form to fit the data:

$$E(z)M_\Delta = M_5 \left(\frac{T}{5\,\mathrm{keV}} \right)^\alpha, \qquad (7)$$

where $E(z)$ is the redshift-dependent Hubble parameter

$$E(z) = \frac{H(z)}{H_0} = \sqrt{\Omega_M(1+z)^3 + \Omega_\Lambda}. \qquad (8)$$

In Equation (7), the mass M_Δ is usually defined as the total mass within the radius, at which the mean density becomes Δ times the critical density. We quote the results for M_{2500} for an easy comparison with previous studies. In our combined sample, 14 clusters have published X-ray temperatures (Table 2) spanning the 1.7 keV $< T <$ 10.4 keV range with
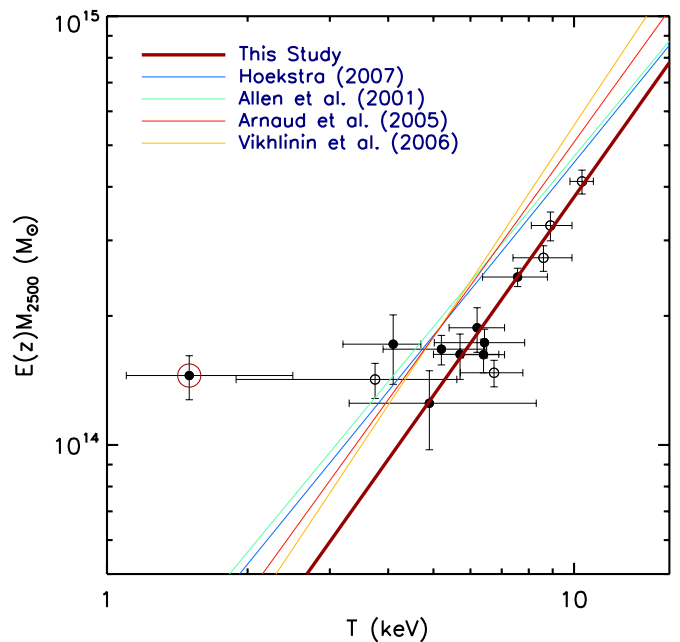

Figure 25. X-ray temperature vs. lensing mass. As in Figure 24, filled and open circles represent the current clusters studied here and the five clusters in our previous publications. The slope of the power law $\alpha = 1.54 \pm 0.23$ ($M \propto T^\alpha$) is consistent with the theoretical prediction 3/2 and also previous results obtained from low-redshift samples. Note that the Hoekstra (2007) relation shown here is the revised result after we applied the 10% reduction in mass as explained in Mahdavi et al. (2008). The greatest outlier from the M–T_X relation is RCS 0439−2904 (red circle), which perhaps is a line-of-sight superposition of multiple components (Cain et al. 2008) boosting the weak-lensing mass measurement without significantly affecting temperature measurement.

(A color version of this figure is available in the online journal.)

reasonable constraints on their uncertainties. For these clusters, we present the mass–temperature relation in Figure 25. The thick red line shows the best-fit power-law relation with $\alpha = 1.54 \pm 0.23$ and $M_5 = (9.13 \pm 0.85) \times 10^{13}\,h^{-1}\,M_\odot$. The cluster RCS 0439−2904 (marked with red circle) is a significant outlier from this relation and the fit shown here is obtained without including this cluster. The exclusion of this cluster in our estimation of the M–T relation is justified because there is a strong indication that RCS 0439−2904 might be a line-of-sight superposition of multiple clusters (Section 3.3). However, we stress that adding RCS 0439−2904 does not change our results (reducing the slope to 1.48 ± 0.23).

Allen et al. (2001) studied six relatively relaxed clusters at $z \lesssim 0.46$ observed with *Chandra* and obtained the mass–temperature relation $\alpha = 1.51 \pm 0.27$ and $M_5 = (1.32 \pm 0.13) \times 10^{14}\,h^{-1}\,M_\odot$. Arnaud et al. (2005) used six nearby ($z \lesssim 0.15$) $T > 3.5$ keV clusters observed with *XMM-Newton* and measured the slope $\alpha = 1.51 \pm 0.11$ and the normalization $M_5 = (1.25 \pm 0.04) \times 10^{14}\,h^{-1}\,M_\odot$, which are consistent with the results of Allen et al. (2001). A larger sample from *Chandra* has been studied by Vikhlinin et al. (2006), who analyzed 13 low-redshift clusters in the temperature range 0.7–9 keV. They also agreed that the observed scaling relation is in good accordance with the theoretical prediction, albeit with slightly higher slope 1.64 ± 0.06 than previous X-ray results. Their normalization $M_5 = (1.25 \pm 0.05) \times 10^{14}h^{-1}\,M_\odot$ is in good agreement with previous X-ray results.

Because X-ray studies derive cluster masses from temperature with hydrostatic equilibrium assumption, these results showing

that the correlation is tight and the power-law slope of the M–T_X relation is close to the theoretical prediction 3/2 may not be a direct proof for the cluster self-similarity. It is critical to investigate if the relation still holds when the masses are given by an independent estimator.

The weak-lensing mass versus X-ray temperature relation is investigated by Hoekstra (2007), who derived $\alpha = 1.34^{+0.30}_{-0.28}$ and $M_5 = (1.4 \pm 0.2) \times 10^{14}\, h^{-1}\, M_\odot$ from the 17 clusters at $0.17 \lesssim z \lesssim 0.54$, which are in good agreements with the values from X-ray studies. Mahdavi et al. (2008) updated the redshift distribution used by Hoekstra (2007) and found that the new $n(z)$ from the photometric redshift catalog of Canada–France–Hawaii Telescope Legacy Survey derived by Ilbert et al. (2006) gives on average ∼10% smaller masses. We show this revised result in Figure 25. We further note that Hoekstra (2007) used the ASCA temperatures that do not correct for cool cores. The absence of this cool–core correction can bias the temperatures low.

We verified that the above M–T_X relation is not sensitive to a mass–concentration relation. When we recompute our M_{2500} using the mass–concentration relation of Bullock et al. (2001), the power-law slope α virtually remains the same and the normalization (M_5) decreases ∼3% only. The X-ray and Hoekstra (2007) results were obtained without any assumption on mass–concentration relation. Nevertheless, we tested if the result of Hoekstra (2007) changes when the masses are derived from NFW profile fitting with the Duffy et al. (2008) mass–concentration relation as is done in this paper. Again, we found that neither the normalization nor the slope of the M–T_X relation of Hoekstra (2007) changes because of this mass determination method.

It is easy to see in Figure 25 that there is a 20%–30% discrepancy in normalization between our result and previous results. The discrepancy may imply that the normalization decreases with redshift or our weak-lensing masses are biased low. One cause for possible weak-lensing bias is the redshift estimation bias, similar to the case in Hoekstra (2007). We estimate that the sample variance of the UDF may be responsible for the 5%–12% shift in mass depending on the cluster redshift. However, although we cannot exclude this possibility, this would aggravate the already problematic existence of the most massive clusters in the high-z universe (see Section 5 for details). Therefore, it seems more plausible that there is some evolution in the normalization of the mass–temperature relation to the highest redshifts.

Finally, we compare the masses derived from X-rays and lensing analyses. The cluster masses at r_{200} obtained from the X-ray results are listed in Table 2. We use an isothermal β assumption to derive these values in order to take advantage of the published parameters in the literature. For the clusters that do not have published measurements of their X-ray surface brightness profile (because the S/N of the existing data do not constrain the shape of the X-ray profile well) we assume $\beta = 0.7$. Figure 26 shows the result for 14 clusters in our combined sample. The agreement between the lensing and X-ray estimates is good except for RCS0439−2904, which, as mentioned already, might be a line-of-sight superposition of multiple components (Cain et al. 2008). It is important to remember that an SIS profile is assumed for the derivation of M_{200} from X-ray data. Therefore, it is possible that this excellent agreement might be a coincidence to some extent and a systematic difference might appear if masses are evaluated at different radii.
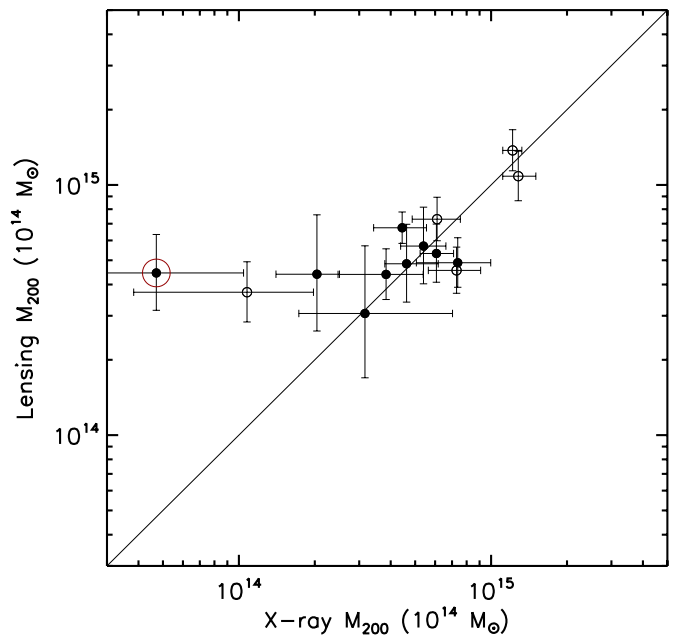

Figure 26. Virial mass comparison between X-ray and weak-lensing results. Not surprisingly, the trends are similar to that of the mass–temperature relation shown in Figure 25. The cluster RCS0439−2904 (red circle) again is the greatest departure from the line of equality. Filled and open circles represent the current clusters studied here and the five clusters in our previous publications, respectively.

(A color version of this figure is available in the online journal.)

5. ABUNDANCE OF THE MOST MASSIVE CLUSTERS AT HIGH REDSHIFT

The abundance of the most massive clusters at high redshift is extremely sensitive to cosmological parameters. In the current era when we can estimate the cosmological parameters to a high precision (mainly from the cosmic microwave background (e.g., Komatsu et al. 2011) and Type-Ia supernova studies (e.g., Amanullah et al. 2010)), discovery of even a single massive cluster can challenge the current ΛCDM model (Mortonson et al. 2011).

In Jee et al. (2009), we presented a weak-lensing analysis of XMM J2235−2557 and found that the mass of the cluster is surprisingly high. With the cosmological parameters fixed at the current best-fit values, the theoretical probability of finding such a massive cluster in the survey volume is only $\lesssim$1%. The exact value for the probability depends on the adopted mass function and cosmological parameters. Nevertheless, independent estimates (e.g., Jimenez & Verde 2009; Sartoris et al. 2010; Holz & Perlmutter 2010) agree that the discovery provides significant tension with the current ΛCDM cosmology. In this section, we extend the study of Jee et al. (2009) to the most massive clusters in our sample with a new mass function, revised survey areas, and marginalization over the uncertainties of cluster masses and cosmological parameters.

5.1. Mass Function

The mass function is often given in the following form:

$$\frac{dn}{d\ln M} = \frac{\rho_{m,0}}{M} \left| \frac{d\ln \sigma(M,z)}{d\ln M} \right| f, \qquad (9)$$

where σ is the rms variation of the density field when smoothed on scale M. $\rho_{m,0}$ is the present matter density. The function f determines the shape of the mass function.

Jenkins et al. (2001) proposed a redshift-independent form $f = f(\sigma)$, which makes the above mass function agree with their numerical simulation results with high precision. Tinker et al. (2008) improve the agreement by considering the redshift-dependence of $f = f(\sigma, z)$, which is expressed as

$$f(\sigma, z) = A\left[\left(\frac{a}{b}\right)^{-a} + 1\right] e^{-c/\sigma^2}, \qquad (10)$$

where $A = 0.186(1 + z)^{-0.14}$, $a = 1.47(1 + z)^{-0.06}$, $b = 2.57(1 + z)^{-0.011}$, and $c = 1.19$ when the mass is defined as the total mass at the radius, inside of which the mean density is 200 times the mean density of the universe at the cluster redshift. We refer to it as M_{200m} when necessary to distinguish it from M_{200}, which is more commonly used to refer to the mass at the radius, where the mean density becomes 200 times the critical density. The deviation of the universality of the mass function by Jenkins et al. (2001) from the numerical simulation results is 20%–50% (Tinker et al. 2008); Bhattacharya et al. (2011) argue that the difference between different fitting formulae is probably larger than the scatter seen in the largest simulations.

5.2. Cluster Survey Area

The cluster survey area that one chooses to adopt to evaluate the cosmological significance for discovery of unusually massive clusters is somewhat controversial. For example, Mortonson et al. (2011) argue that $\sim 300\,\mathrm{deg}^2$ should be used for the search area of XMM2235−2557 at $z = 1.4$ instead of the pilot survey area of $\sim 11\,\mathrm{deg}^2$ (Jee et al. 2009). The argument for this $\sim 300\,\mathrm{deg}^2$ area is based on the study of Hoyle et al. (2011), who assumed $\sim 168\,\mathrm{deg}^2$ for XCS, $\sim 64\,\mathrm{deg}^2$ for *XMM*-LSS, $\sim 11\,\mathrm{deg}^2$ for XDCP, $\sim 17\,\mathrm{deg}^2$ for WARPS, and $\sim 33\,\mathrm{deg}^2$ for RDCS. However, the different *XMM-Newton*-based surveys overlap significantly. In addition, because the flux limit that enables a secure cluster detection at $z > 1$ is $\sim 10^{-14}\,\mathrm{erg\ cm}^{-2}\,\mathrm{s}^{-1}$, the effective search area must be reduced significantly. For example, the XDCS survey has continued since the end of the 11 deg² pilot survey and now reaches $\sim 50\,\mathrm{deg}^2$ (R. Fassbender 2011, in preparation) for a flux limit of $\sim 10^{-14}\,\mathrm{erg\ cm}^{-2}\,\mathrm{s}^{-1}$. The RDCS survey covers a geometrical area of 50 deg² only at relatively high fluxes. However, the area suitable for $z > 1$ cluster detection is $\sim 5\,\mathrm{deg}^2$, corresponding to fluxes below $\sim 3 \times 10^{-14}\,\mathrm{erg\ cm}^{-1}\,\mathrm{s}^{-1}$ (Rosati et al. 1998). Considering the argument listed above, the combined survey area for the X-ray-selected high-z clusters should be $\sim 100\,\mathrm{deg}^2$.

5.3. Abundance Estimation and Eddington Bias

In the full sky survey, the number of clusters with mass and redshift greater than M_{min} and z_{min}, respectively, is given by

$$N(M, z) = \int_{z_{min}}^{z_{max}} \frac{dV(z)}{dz} dz \int_{M_{min}}^{M_{max}} \frac{dn}{dM} dM, \qquad (11)$$

where dV/dz is the volume element and dn/dM is the mass function. For massive high-redshift clusters, the result is sensitive to the mass function dn/dM near z_{min} and M_{min}.

We compute the probability of finding each cluster by marginalizing over the measurement errors, assuming a log-normal distribution for $P(M)$. This is different from the approach of Jee et al. (2009), where we simply used a threshold mass M_{thr} to evaluate the integral (Equation (11)). Nevertheless, we emphasize that the new method yields values very close to

those obtained from the previous method when the mass uncertainty is relatively small ($\lesssim 20\%$). For example, marginalizing over the measurement error gives an abundance of $\sim 2 \times 10^{-3}$ for XMM J2235−2557 in the original 11 deg² XDCP survey, which is in good agreement with the previous value of $\sim 5 \times 10^{-3}$. As we use a fixed value of z_{max}, the resulting abundance is slightly conservative because in principle the maximum redshift should decrease at the low end of $P(M)$; remember that at the high end of $P(M)$, the steep mass function cancels the effect of increased z_{max}. For the conversion from expected number to probability we assume Poissonian distribution. That is, if the expected number is N within a particular survey, the discovery probability is simply $P = 1 - e^{-N}$.

Mortonson et al. (2011) noted that an Eddington bias (Eddington 1913) is an important factor in the discussion of the cosmological significance using most massive clusters. Eddington bias is the combined effect of a steep mass function and measurement uncertainty. For example, consider the weak-lensing mass estimate of XMM2235 of $M_{200} = (7.3 \pm 1.3) \times 10^{14}\,M_\odot$. Because the slope of the mass function near the cluster mass is steep, there should be more $\lesssim 7.3 \times 10^{14}\,M_\odot$ objects scattering up than $\gtrsim 7.3 \times 10^{14}\,M_\odot$ objects scattering down. As a matter of course, this does not mean that XMM2235's mass should be quoted with a lower mass (for individual clusters the scatter is symmetric). However, when we discuss the existence of the cluster in probabilistic terms, this additional chance of bias should be considered from a Bayesian point of view.

We adopt the convenient Mortonson et al. (2011) prescription, which is to replace the observed mass with the following reduced mass M' in the estimation of the abundance: $M' = \exp(1/2\gamma\sigma_{\ln M})M$, where γ is the local power-law slope ($dn/d\ln M \sim M^\gamma$) and $\sigma_{\ln M}$ is the 1σ uncertainty of $\ln M$ (log-normal distribution is assumed for mass errors).

5.4. Probability of Discovery for Most Massive Clusters

In Figure 27 and Table 3, we show the discovery probability of all clusters (i.e., similarly massive clusters) studied in this paper. We compute the probabilities after marginalizing over the Wilkinson Microwave Anisotropy Probe 7 year (WMAP7) Monte Carlo Markov Chain data.[18] The probabilities estimated within the parent survey may lead to a somewhat aggressive interpretation for some clusters. For example, most of the RDCS clusters have significantly low probabilities mainly due to the small ($\sim 5\,\mathrm{deg}^2$) survey area. However, most non-X-ray-selected clusters (ISCS and RCS) have discovery probability equal or close to unity even within their parent surveys.

As mentioned in Section 5.2, we believe that the survey area of 100 deg² is still a conservative choice for most of the clusters shown here (the exceptions are MS1054−0321 and CL J0152−1357, which were discovered in the EMSS $\sim 735\,\mathrm{deg}^2$ survey). With this survey area, there remain four clusters whose discoveries are still unusual given our current understanding of cosmological parameters (the names of these clusters are shown in Figure 27). The cluster with the lowest probability ($\sim 1\%$) is the $z \sim 0.9$ cluster CLJ1226+3332, whose weak-lensing mass and X-ray temperature are $M_{200m} \sim 1.6 \times 10^{15}\,M_\odot$ and $T_X \sim 10\,\mathrm{keV}$, respectively. Because the cluster was discovered in a 72 deg² survey (WARPS), using 100 deg² does not increase the probability significantly. In addition, *XMM-Newton* archival search programs look for regions where no known X-ray

---

[18] Available at http://lambda.gsfc.nasa.gov/product/map/current/params/lcdm_sz_lens_wmap7.cfm.
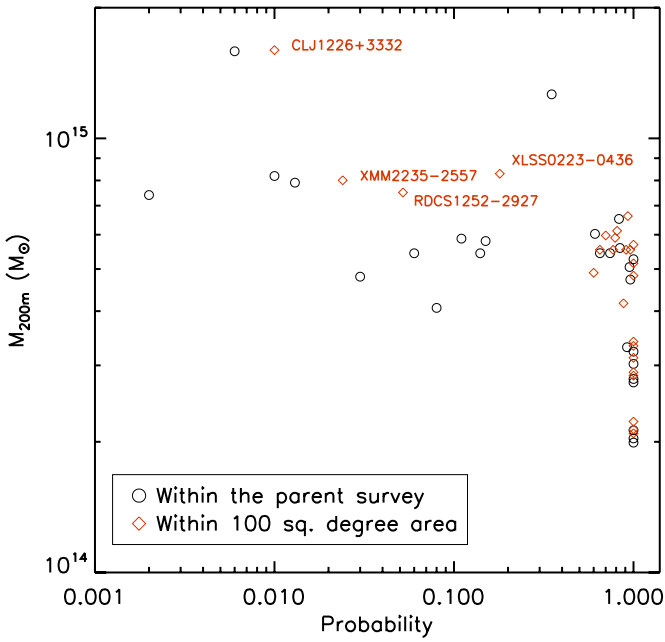
Figure 27. Discovery probability of clusters. After applying Eddington bias to the lensing masses, we marginalize over the uncertainties of the WMAP7 cosmological parameters in order to estimate the discovery probability. MS 1054−0321 and CL J0152−1357 were discovered in the Einstein Medium Sensitivity Survey (EMSS), which covered a total of 778 deg² (Gioia et al. 1990). We do not recompute the probability for these two clusters with 100 deg².

(A color version of this figure is available in the online journal.)

Table 3
Discovery Probability of Galaxy Clusters

Cluster Name	Within Parent Survey	100 deg²
XMMXCS J2215−1738	0.96	1
XMMU J2205−0159	1	1
XMMU J1229+0151	0.61	0.81
WARPS J1415+3612	0.65	0.96
ISCS J1432+3332	0.14	0.77
ISCS J1429+3437	0.15	0.79
ISCS J1434+3427	1	1
ISCS J1432+3436	0.11	0.70
ISCS J1434+3519	1	1
ISCS J1438+3414	0.92	1
RCS 0220−0333	0.74	0.91
RCS 0221−0321	1	1
RCS 0337−2844	0.84	1
RCS 0439−2904	0.95	1
RCS 2156−0448	1	1
RCS 1511+0903	1	1
RCS 2345−3632	1	1
RCS 2319+0038	0.83	0.93
XLSS J0223−0436	0.01	0.18
RDCS J0849+4452	0.03	0.60
RDCS J0910+5422	0.06	0.65
RDCS J1252−2927	0.002	0.052
XMMU J2235−2557	0.013	0.024
CL J1226+3332	0.006	0.01
MS 1054−0321	0.35	. . .[a]
CL J0152−1357	1	. . .[a]
RDCS J0848+4453	0.08	0.88

Note. [a] MS 1054−0321 and CL J0152−1357 were discovered in the Einstein Medium Sensitivity Survey (EMSS), which covered a total of 778 deg² (Gioia et al. 1990).

luminous clusters exist, and thus the search volume in the *XMM-Newton* archival survey excludes the $z \lesssim 1$ volume by observer's selection. This makes our probability estimation for CLJ1226+3332 even more conservative. The second lowest probability is found with XMM2235−2557 at $z = 1.4$. The probability of ∼3% is much higher (after the area and Eddington bias correction) than our previous value of ∼0.5% within the 11 deg² pilot XDCP survey, but still gives ∼2σ tension with the predicted number of clusters from ΛCDM. RDCS1252−2927 at $z = 1.24$ is ranked as third in rarity, giving $P \sim 6\%$, which is followed by XLSS0223−0436 at $z = 1.22$ ($P \sim 18\%$).

Combining discovery probabilities of all our clusters is somewhat tricky. Because of Poissonian fluctuation, the discovery probability is always lower than the estimated abundance (i.e., $P = 1 - e^{-N}$). For example, if the expected number of a given cluster is $N = 1$ within 100 deg² survey, the probability is ∼0.63. Obviously, simply multiplying probabilities of all clusters potentially leads to an unreasonably low final value if there are many slightly less-than-one-probability clusters. Nevertheless, if we include only rare clusters ($P \ll 1$), multiplying individual probabilities provides a useful measure on how much the existence of these multiple clusters give rise to tension with the current cosmological parameters.

One set of cosmological parameters that increase the predicted abundance of one massive cluster can boost another similarly massive cluster's abundance. Therefore, multiplication of probabilities must be done separately for each chain, and the final probability should be obtained after properly taking into account each chain's weight. We find that the final combined probability obtained in this way is ∼0.03%.

5.5. Exclusion Curve Test

Mortonson et al. (2011) presented fitting formulae, which provide an exclusion mass as a function of redshift for given sample and parameter variance confidence limits (CLs). Even a single cluster equal to or above the exclusion mass rules out both ΛCDM and quintessence.

In Figure 28, we compare our clusters to the exclusion curves of Mortonson et al. (2011). Although we believe that the proper choice for the sky area is 100 deg² or less, we also plot the result for the 300 deg² assumption, which was adopted in Mortonson et al. (2011). For simplicity, we only consider the case where the sample variance CL is equal to the parameter variance CL, which is referred to as joint CL in Mortonson et al. (2011).

The central mass of the cluster CL J1226+3332 after the Eddington bias correction lies above the joint CL 95% exclusion curve when we adopt 100 deg² for the survey area. All the masses of the four clusters shown here are approximately on or above the joint CL 80% exclusion curves. When we consider 300 deg² for the search area instead, we note that the two clusters CLJ1226+3332 and XMM J2235−2557 are above the 80% exclusion curves. We clarify here that Mortonson et al. (2011) used the mass of XMM J2235−2557 reported by Stott et al. (2011), whose value is similar to our weak-lensing mass, but has significantly larger uncertainty (∼40%); Stott et al. (2011) derived the cluster mass from their X-ray scaling relation. This large uncertainty leads to ∼40% Eddington bias, and Mortonson et al. (2011) concluded that the resulting mass of the cluster provides only a negligible tension with ΛCDM when they assume 300 deg² for the sky area. On the other hand, our mass uncertainty is ∼18%, and the corresponding Eddington bias is ∼12%, which makes the corrected mass still close to the ∼85% exclusion curve for Mortonson et al. (2011)'s 300 deg² assumed area.
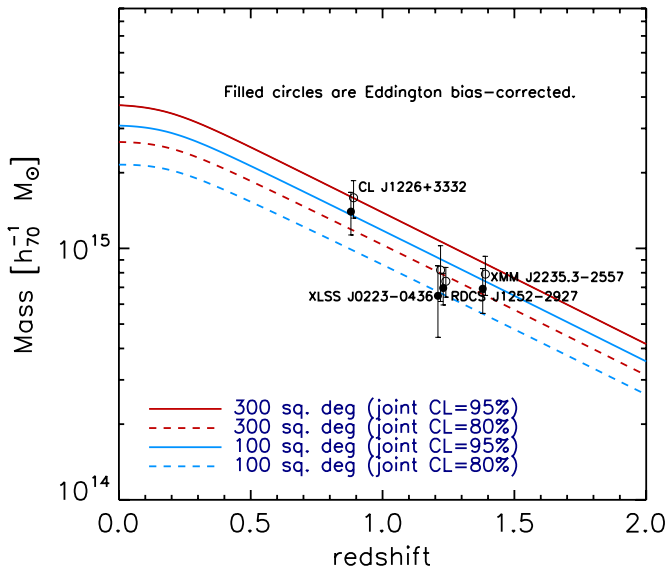
Figure 28. Exclusion curves. Any cluster's mass above the given curve excludes the ΛCDM with the joint CL specified (Mortonson et al. 2011). For example, the central value (Eddington-bias corrected) of CL J1226+3332 rules out $\gtrsim$95% of currently allowed ΛCDM models at the $\gtrsim$95% confidence level for the 100 deg^2 area.

(A color version of this figure is available in the online journal.)

The above exclusion curve test provides weaker constraints when one is using more than a single cluster to examine their cosmological significance because the tool adopts the lowest redshift for the sample in the estimation of the cluster abundance (Mortonson et al. 2011). Therefore, we do not attempt to estimate the tension by combining the four most massive clusters.

5.6. Interpretation of Overabundance of Massive Clusters at High Redshift

Assuming the current well-accepted ΛCDM cosmology, we have demonstrated above that the discovery of the most massive clusters in our sample are rare events. Among the most popular interpretation would be that the primordial density fluctuation is non-Gaussian. For example, Jimenez & Verde (2009) claim that the local f_{NL} should be in the range of 150–260 to accommodate XMMU2235−2557 within the pilot 11 deg^2 survey. We suspect that their estimate of f_{NL} would decrease somewhat when both the Eddington bias and revised area of 50–100 deg^2 are taken into account. A tighter constraint is possible if one utilizes the weak-lensing masses of the four most massive clusters studied here. A similar study is performed by Hoyle et al. (2011) from the investigation of the 14 high-redshift cluster masses reported in the literature, giving a significantly large $f_{NL} > 375$ (after marginalization over WMAP5 parameters).

One crucial test that however should accompany these non-Gaussianity studies is the investigation of the mass function at the high mass end. The existing limited-volume simulations do not constrain the number density of extremely massive clusters accurately, and the commonly used fitting functions are simply extrapolated results in this regime. Another potentially important contribution from numerical simulation is the predicted mass function specific for a given survey, which takes into account the various aspects of selection limits and projection effects.

The projection effect is always a concern in the cosmological interpretation of extremely massive clusters. Certainly, a superposition of two moderately massive clusters or a long filament viewed along the line of sight can be identified with an extreme object. The former case is easily detected by a redshift histogram if the field is spectroscopically surveyed. Initially, RDCS1252−2927 at $z = 1.24$ was such a candidate because the redshift catalog showed three possible foreground groups at $z = 0.47$, 0.68, and 0.74 (Lombardi et al. 2005). However, the spatial distributions of these groups are not compact, and they appear to be just loose galaxy groups commonly found in any random field. The latter case (a filament viewed along the line of sight) is very difficult to prove (or disprove) directly. Nevertheless, there are a few circumstantial lines of evidence, which help us to infer if a system possesses extreme triaxiality. Comparing X-ray temperature with weak-lensing mass is useful because a severe triaxiality will give rise to much higher weak-lensing mass than what the temperature predicts. In addition, a line-of-sight elongation inflates velocity dispersion, and the result will be significantly larger than what the lensing predicts. XLSS0223−0436 is potentially such an object because our lensing mass of $M_{200} = 7.4^{+2.5}_{-1.8} \times 10^{14} \, M_\odot$ is much larger than what the X-ray temperature of $\sim$3.8 keV (Bremer et al. 2006) suggests. However, the X-ray photon statistics are poor, and Bremer et al. (2006) could not determine an upper limit of the X-ray temperature. Deeper *Chandra* observations would be necessary to robustly examine this large (a factor of 2–3) discrepancy. We note that the existing data for CLJ1226+3332 and XMM J2235−2557, the two clusters with the largest tension with ΛCDM in our sample, do not suggest the possibility that weak-lensing masses are significantly boosted by any projection effect.

6. SUMMARY AND CONCLUSIONS

We have presented a weak-lensing analysis of 22 high-redshift ($0.91 < z < 1.46$) clusters using *HST*/ACS images. Most clusters in the sample show a significant lensing signal and are well detected in our two-dimensional mass reconstruction. We complement our sample with five high-redshift clusters that were studied in the past in order to compare lensing results with X-ray and dynamical measurements over a large range of masses and to discuss the most massive clusters in this combined sample in the context of cosmology. Our results are summarized as follows.

1. The dynamical velocity dispersions are consistent with the values estimated by lensing analysis.
2. The power-law slope of the lensing-mass–temperature relation is in good agreement with the theoretical prediction, which is also supported by previous investigations carried out with X-ray data alone or with both X-ray and lensing data.
3. We see evidence of an evolving normalization constant in the $M−T_X$ relation.
4. The masses derived from X-ray and lensing measurements are in good agreement.
5. The existence of the most massive clusters in our sample gives rise to tension with the current ΛCDM standard structure formation paradigm.

The first conclusion is consistent with the findings of Hoekstra (2007) who studied low-redshift clusters. Our result demonstrates that the relation can be extended to this high-redshift regime, albeit with slightly increased scatter. This larger scatter could be intrinsic for high-redshift clusters, which are likely to

possess more merging substructures than low-redshift systems. However, one must remember that most clusters in our sample do not yet have a sufficient number of spectroscopic members to give reliable estimates. In addition, the depth of the ACS images is also less than optimal in many cases, which increases uncertainties for the lensing values. Our assumption of SIS in the derivation of the velocity dispersion may introduce some bias in the relation simply because the real clusters are not singularly isothermal. Nevertheless, the collective behavior of the relation being consistent with the equality is still noteworthy and hints at the possibility that the dynamical measurements from a large number of cluster members may still serve as useful proxies for masses in this redshift regime.

The mass–temperature relation presented here is tight, particularly for hot clusters. The current result indicates that the power-law slope of the mass–temperature relation does not evolve since $z \sim 1$. However, our normalization value is 20%–30% lower than previous results, suggesting that the X-ray temperatures of the clusters at $z \sim 1$ may be systematically higher than at low redshifts. The shift can imply that non-thermal sources of heating (e.g., merging, active galactic nucleus activity, etc.) might be more prevalent at higher redshifts or simply the difference in gas fraction (because of different cluster formation epoch) might be significant. Alternatively, one can also consider bias in our lensing analysis. However, it is very unlikely that our calibration error, even at a maximum, can induce 20%–30% systematic errors. Our shear calibration error verified by numerical simulations is at most at the $\sim$1% level. The redshift estimation bias (i.e., the magnitude versus redshift relation in the UDF does not represent the mean relation of the universe) is at the 5%–12% level for each cluster, giving the highest error for the most distant object. Most importantly, if the cluster masses in our sample should be somehow increased by 20%–30%, this would not only degrade the dynamic versus lensing velocity dispersion relation substantially, but also make the existence of the most massive clusters much more problematic with the current cosmological parameters.

The fourth conclusion is somewhat foreseen by the tight mass–temperature relation. However, this direct comparison of mass between X-ray and lensing methods provides another way to verify our normalization in the M–T relation. Again, the clusters with the lowest temperatures are the greatest outliers from the equality. On the other hand, the other relatively massive clusters give consistent results between X-ray and lensing measurements. When we repeat the analysis by re-calculating the cluster mass at smaller radii (e.g., M_{500} instead of M_{200}), the relation virtually remains the same. This indicates that the difference in the assumption of the cluster mass profile (i.e, isothermal β versus NFW) is not a significant source of bias between the two measurements.

Finally, the last conclusion is the most striking finding of the current investigation. The above studies on the relations between lensing mass and other properties do not support the possibility that our lensing mass determination is significantly biased high. A significantly high degree of non-Gaussianity or high value of σ_8 may explain the existence of these massive clusters at high redshift. However, we caution that our current theoretical knowledge of the mass function at the high end is limited by small number statistics.

Foley et al. ([2011]) reported the discovery of SPT-CL J2106−5844, which is claimed to be the most massive cluster known at $z > 1$ based on the X-ray temperature and Sunyaev–Zel'dovich measurement. The authors estimate that there is only a 7% chance of finding such a massive cluster within the 2500 deg^2 survey area. The mass of the cluster still needs to be verified by other methods (e.g., weak lensing analysis). However, if the cluster is indeed as massive as reported, the existence of SPT-CL J2106−5844 also favors our claim that the most massive clusters at high redshift provide non-negligible tension with our current understanding of structure formation.

APPENDIX A

PSF MODELING

The importance of accurate removal of PSF effects cannot be stressed too much in weak-lensing analyses. Both dilution and bias of shear signals must be accounted for with rigor in order to advance from mere detection into measurement. One difficulty in ACS PSF modeling is the small field of view ($3' \times 3'$), which does not provide a sufficient number of high S/N stars. Because ACS PSFs vary with time and position, it is not possible to interpolate/extrapolate the PSF information reliably based on a few tens of stars on a target image. Fortunately, the PSF pattern in ACS seems to be repeatable. That is, one can find two or more observations remote in time but closely related to each other in the behavior of the PSF pattern (Jee et al. [2007b]). Therefore, it is possible to use a limited number of stars on one image, find another image possessing a similar PSF pattern but instead with many more stars covering the entire field, and utilize this second image to infer the PSF in the first image. In practice, a slight complexity arises because in general a target field is visited with many telescope pointings that are different not only in shift and rotation, but also in PSF pattern. Therefore, one needs to determine PSF patterns for individual pointings first and then apply shift and rotation to model the PSFs on the final mosaic image.

The above method has been successfully applied to our previous *HST* weak-lensing analysis of clusters. We refer readers to those papers (e.g., Jee et al. [2009]) for details. Here, we only summarize the PSF modeling procedure for the current data sets. We use the Jee et al. ([2007b]) PSF library, which provides a polynomial description of two-dimensional PSF variations
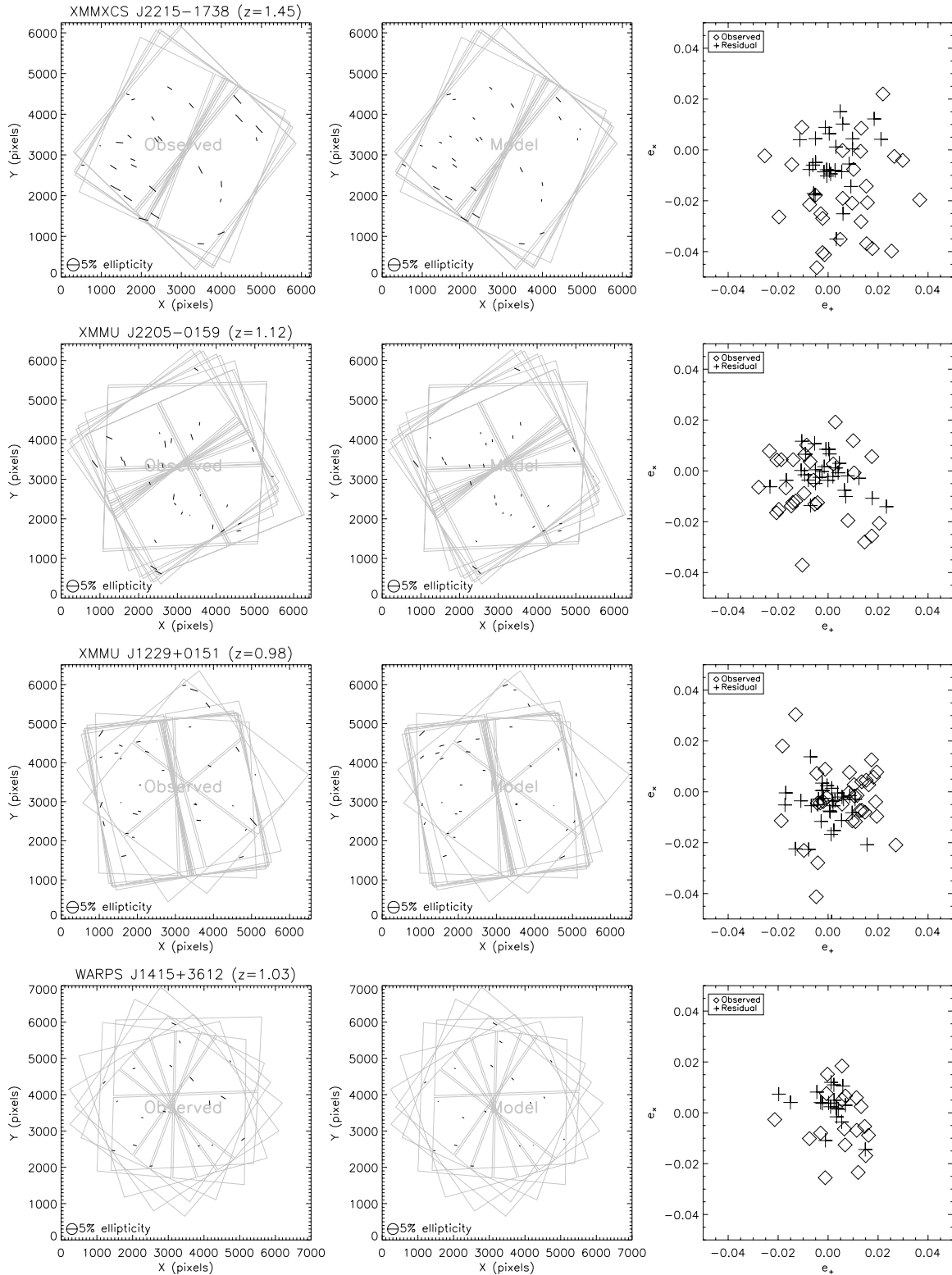
Figure 29. Point-spread function correction. The left panels show the observed ellipticity pattern of the stars whereas in the middle panels we display the reconstructed ellipticity pattern at the location of the stars. The right panels compares the two ellipticity components e_+ and $e_\times$ before and after the correction.

based on principal components analysis (PCA). This PCA method allows us to obtain compact basis functions to describe the spatial variation of PSFs (Jee et al. 2007a; Jee & Tyson 2011).

We identified stars on each cluster observation using the objects' size and magnitude. The best PSF template for each

cluster observation frame was determined by comparing both size and ellipticity of these stars. We stored the name of the template and the alignment information (i.e., shift in pixels and rotation angle in degrees). After completing this task, we then went through objects in the source catalog that is created from the final stack, computed their location within each input frame,
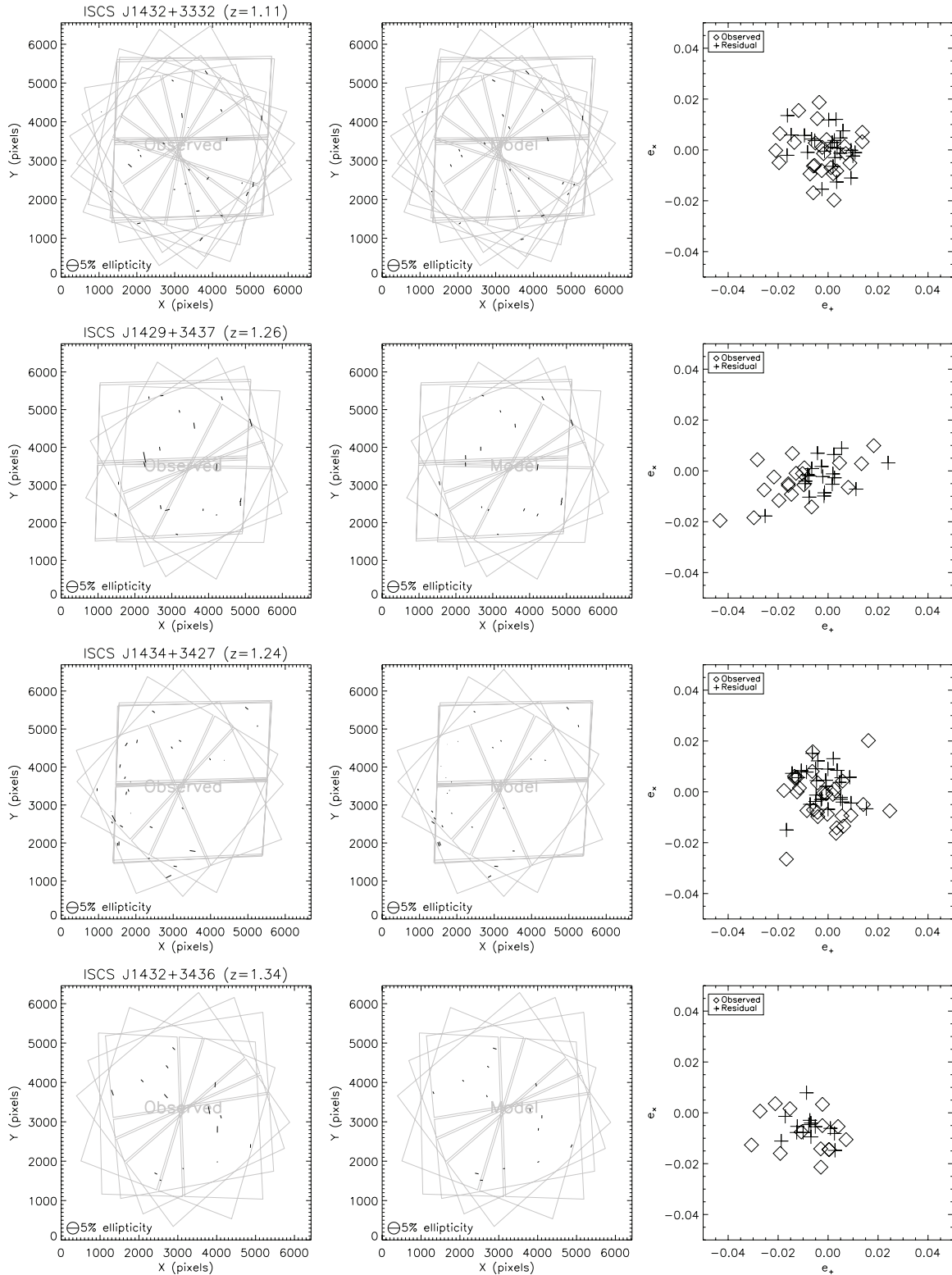
Figure 29. (Continued)

and interpolated the coefficients of the principal components at the location. These coefficients were transformed to two-dimensional PSF images, which were stacked to generate the final PSF model after proper rotation was applied; in fact, the CTI correction (see Section B) was made prior to stacking by stretching the individual PSFs in the direction of CTI trail.

In Figures 29, we show the PSF correction results. We note that the observed PSF ellipticity on the stack is on average smaller than the typical value because of the rounding effect from field rotation. The rms residual per cluster is less than 1%. Despite some occasional small mismatches, the current level of the PSF correction exceeds the requirement for cluster lensing analysis.
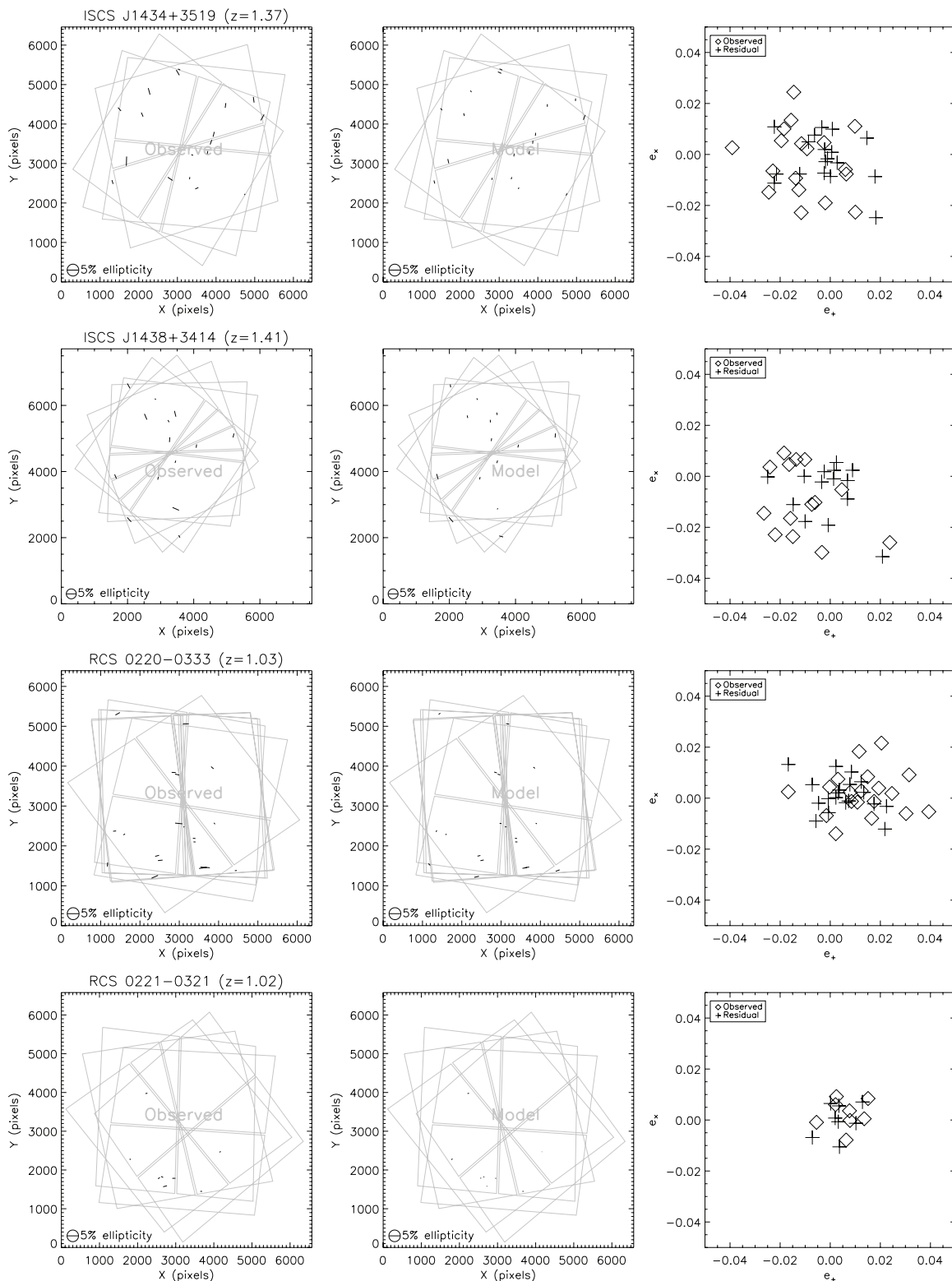
Figure 29. (Continued)

APPENDIX B

CTI CORRECTION

During a CCD readout, some fraction of the charge is trapped because of defects in the silicon. These trapped charges are soon released after a characteristic time τ. This cycle of trap-release events continues until the charges in the last row are transferred. This artifact is sometimes clearly visible as "charge trails."

The *HST*/ACS CTI worsens with time because the number of defects in the CCD is proportional to the amount of the time exposed to the radiation-rich space environment. Most of the cluster images in our program are obtained during the year 2006 (four years after the installation of ACS), and thus we expect the CTI to be much worse than in our previous studies.

Obviously, the effect is undesirable in most applications of the data. The effect is particularly undesirable in weak-lensing
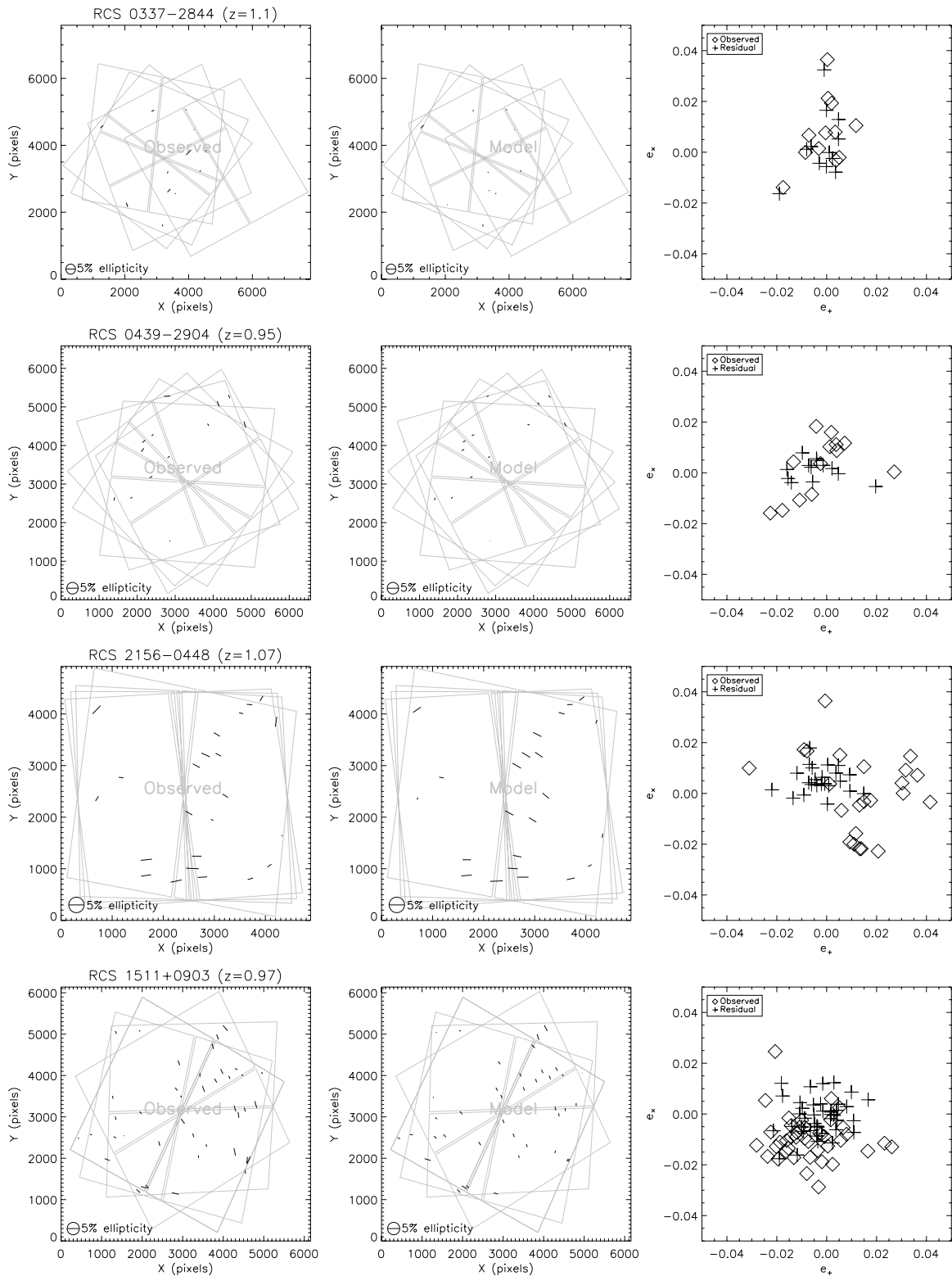
Figure 29. (Continued)

measurements, where one is looking for a subtle distortion of small galaxies. In this analysis, the CTI-induced elongation must be carefully measured and accounted for.

In the characterization of the CTI, we categorize the methods in the literature into four schemes.

1. Difference photometry.
2. Pixel Response measurement.

3. Ellipticity bias of astronomical objects.
4. Ellipticity bias of sub-seeing features (e.g., cosmic ray, hot or warm pixels, etc.).
5. Pixel level correction.

Method 1 utilizes the fact that the CTI-induced elongation leaves some fraction of the charge outside the aperture. Because the fractional loss depends on the CTI, in this scheme an object
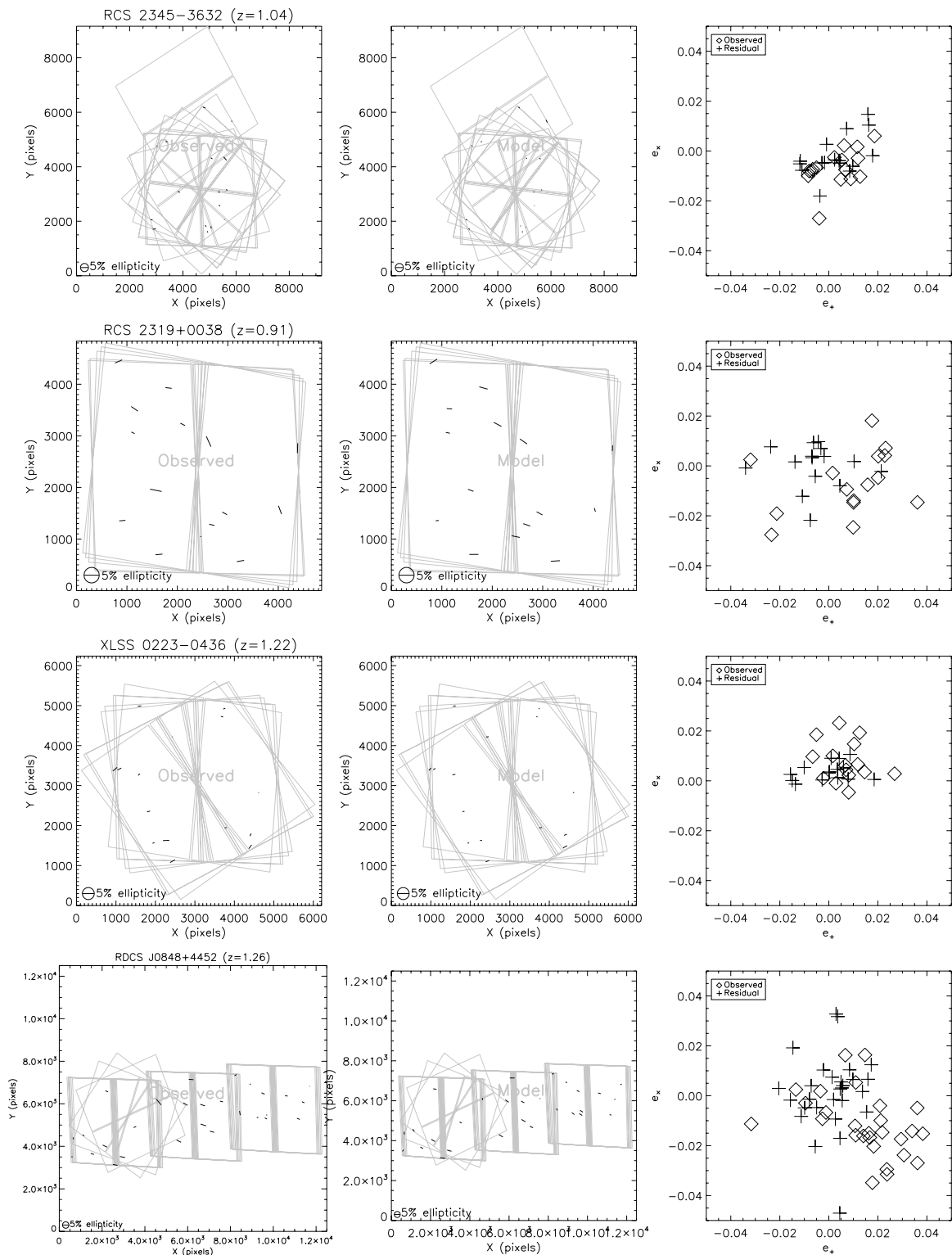
Figure 29. (Continued)

should be observed multiple times in different conditions (e.g., background, time, row, column, etc.). Therefore, this method requires large amounts of well-planned, dedicated observations (e.g., Riess & Mack 2004). This scheme is also useful when one's interest is limited to photometric correction of the CTI effect. Method 2 involves uniformly illuminating a CCD and measuring deviations from that uniformity in the few pixels

farthest from the readout register. A series of programs for First Pixel Response and Extended Pixel Edge Response monitoring have been carried out (Prop. ID 9649, 10044, 10369, and 10732). A similar but more elaborate measurement of this kind is possible if the CCD is exposed to a number of point sources (i.e., single pixel events created by a controlled X-ray source). However, this radiation test is only possible on the
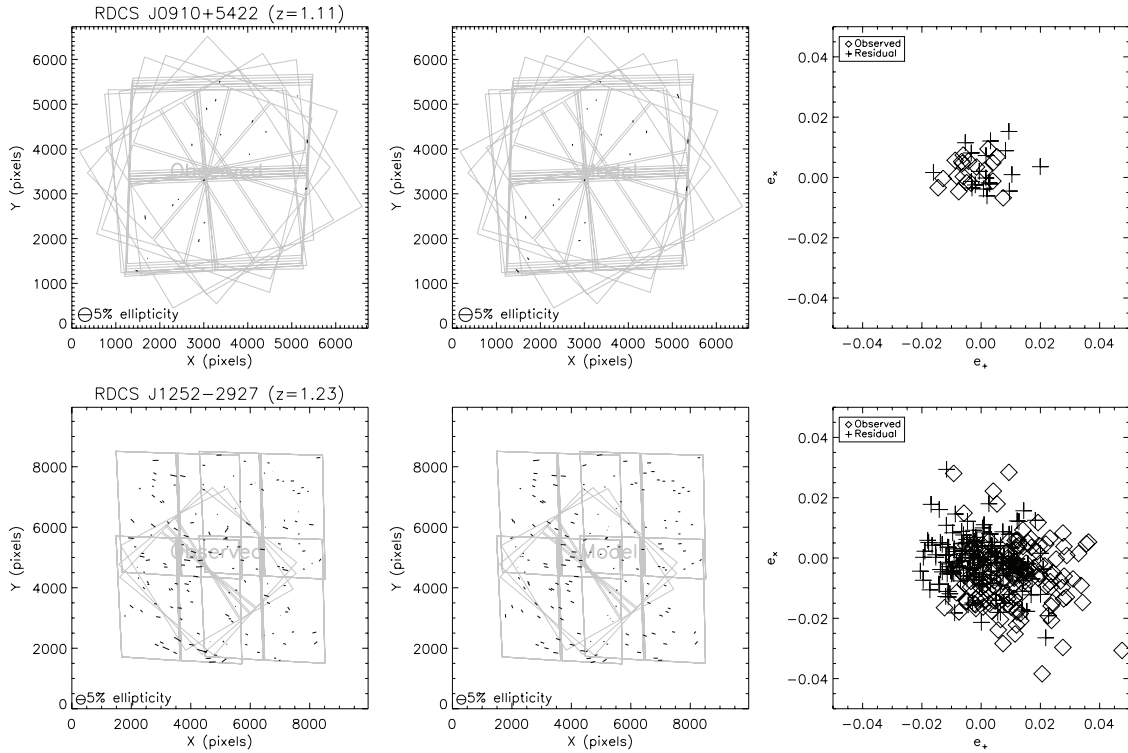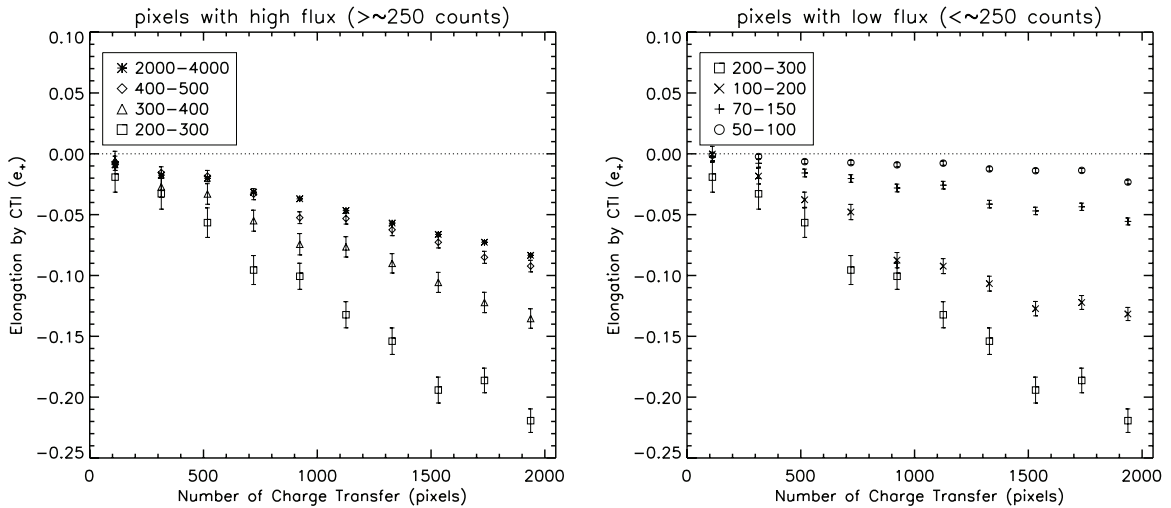
Figure 29. (Continued)

Figure 30. CTI trail of SSFs in the XMMXCS J2215−1738 ACS images. The ellipticity bias (i.e., elongation along the parallel readout direction) due to CTI linearly increases (becomes more negative) with the number of charge transfers. We divide the cases into two groups according to their fluxes in order to demonstrate the different flux-dependence. For the pixels with high counts (left), we observe that the CTI worsens for decreasing fluxes, as was reported in previous studies. However, the trend is reversed for the pixels with low counts (right).

ground. Methods 3 and 4 rely on the fact that for ACS, the CTI-induced elongation is mostly significant along the parallel charge–transfer direction (i.e., the *y*-axis in CCD coordinates). Therefore, taking the average over a number of measurements should reveal the net CTI effect. When employing Method 3, one has to ensure that the shapes of the employed objects are free from other systematic effects (e.g., Schrabback et al. 2010; Hoekstra et al. 2011). For example, poor PSF modeling can induce a residual shape bias that is similar to the CTI-induced distortion in both direction and flux-dependence. Method 4 differs from Method 3 in that the ellipticity bias is measured

from cosmic rays or warm pixels, whose shapes are not subject to geometric distortion or PSF. Because these sub-seeing features are numerous even on a single 500 s exposure image, it is possible to obtain high S/N information on CTI from the data themselves. We applied this method to the weak-lensing analysis of the then highest redshift cluster XMM2235 at $z = 1.4$ (Jee et al. 2009). As Jee et al. (2009) were somewhat not explicit on how to relate the measured ellipticity bias of cosmic rays to object ellipticity, we provide details in the present paper. Method 5 is recently suggested by Massey et al. (2010) and Anderson & Bedin (2010). This approach aims to restore CTI

trails back to the original pixels based on profile measurements of warm pixels. Potentially, this method provides convenient CTI-corrected images, which astronomers can work on directly without worrying about the details of the model. However, the fidelity of the method has yet to be tested.

B.1. Quantification of CTI Effect

Any significant sub-seeing features (hereafter SSFs) present in the raw CCD images are mostly cosmic rays, warm/hot pixels, or simply photon noise, which are commonly removed through elaborate image processing. However, knowing that these SSFs are not caused by the photons following the regular optical path of the instrument, we can use these otherwise nuisance features to our advantage. Because position angles of the SSFs in principle should possess no preferred direction on the surface of the CCD, any deviation from the anticipated isotropy is a clean indicator of the artifact in CCD readout.

We used SExtractor to detect SSFs by looking for objects whose half-light radius is less than 1 pixel. We did not let SExtractor filter the images with matched-PSFs, and thus most of these SSFs would have occupied ~1 pixel if there had been no CTI trails. We also measured the ellipticity of the SSFs by evaluating the unweighted moments using the unfiltered images. This ellipticity measurement scheme is different from Jee et al. (2009), where we measured the ellipticity after the image was convolved with a Gaussian function matching the instrument PSF. The qualitative behavior of the CTI does not change by this difference in measurement scheme. However, the current measurement more clearly reveals the "turnaround" feature that we discuss below.

As a case study, we display the ellipticity bias of the SSFs in the galaxy cluster XMMXCS J2215−1738 in Figure 30. The left and right panels show the results for the SSFs, whose fluxes (counts) are high and low, respectively. Although here we use the SSFs detected only in the images of XMMXCS J2215−1738, they are still numerous and thus enable us to characterize the behavior of the CTI with high significance. First, it is clear that the average ellipticity of the SSFs in each flux range linearly increases (thus more negative) with the number of charge transfer. Second, for the bright SSFs, the CTI effect worsens for decreasing fluxes. In contrast, this trend is reversed for low-flux SSFs. This CTI turnaround was first reported in Jee et al. (2009) through both the SSF analysis and stellar photometry. Schrabback et al. (2010) also observed this turnaround in their independent CTI analysis. It is worth noting that the XMMXCS J2215−1738 cluster was observed in the year 2006 in short (~500 s) exposures, and the background level is very low (~0 counts), which explains the severe CTI trails.

One way to compress the information in the two panels in Figure 30 is to plot the slopes of the data points as a function of flux as shown in Figure 31.[19] The plot helps us to realize how sensitive the CTI slope is to the flux. It is especially remarkable that the CTI turnaround is very sharp (compare this with Figure 4 of Jee et al. 2009).

Before we proceed further, it is instructive to estimate what magnitude range of galaxies is mostly affected by this CTI pattern. As is mentioned in Section 2.2, we select 24–28 mag galaxies as source objects. Considering that the average exposure time is ~500 s and the mean FWHM of the source
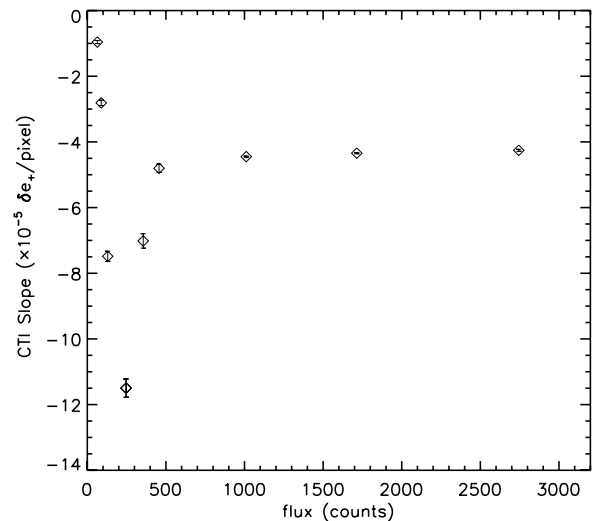
---

[19] When the slope is multiplied by 2048, the result gives the maximum ellipticity bias farthest from the readout register.

Figure 31. CTI slope vs. flux. Here we compress the information in the two panels in Figure 30 into one by plotting the slopes as a function of the fluxes. It appears that the flux-dependence can be classified into three regions. In the high-flux regime ($\gtrsim 500$), the slope changes very slowly with flux. In the intermediate-flux regime ($250 \lesssim$ counts $\lesssim 500$), there shows a precipitous decline of the CTI slope (more elongation) for decreasing flux. Finally, in the low-flux regime ($\lesssim 250$), a sharp turnaround is observed. We found that most of our background galaxies belong to the low end of this regime. Hence, the CTI effect is negligible for our source population.

galaxies is significantly larger than the SSFs (~8 pixels versus ~1.7 pixels), we estimate that this magnitude range corresponds to 2–100 counts in Figure 31. Therefore, the brightest and farthest (from the readout register) galaxies in our source sample suffer the most CTI degradation.

B.2. CTI Correction to Galaxies

We characterize the CTI with the ellipticity bias of the SSFs. Then, a nontrivial question is how to quantitatively relate this ellipticity bias to galaxy ellipticity change. Obviously, the ellipticity bias in SSF is a significant exaggeration of what occurs to galaxy shapes; a small CTI trail induces much larger ellipticity to a δ-function-like feature than to, for example, a $0\farcs5$ galaxy. The exact translation requires our knowledge of the shape of the CTI-induced trail and the surface brightness profile of galaxies. Consequently, the recovery of the galaxy shape prior to the CTI effect involves the same delicacies in PSF-effect correction, which is a more familiar problem.

Indeed, the CTI trailing can be treated as convolution with a one-dimensional kernel, which further smears the post-seeing objects, but only along the readout direction,

$$o(x, y) = i(x, y) \otimes p(x, y) \otimes c(x, y) = i(x, y) \otimes r(x, y), \quad \text{(B1)}$$

where $i(x, y)$ and $o(x, y)$ are the intrinsic and observed images, respectively. $p(x, y)$ and $c(x, y)$ are the convolution kernel representing the PSF and the CTI trailing, respectively. Because the associative law holds for convolution, the smearing of the object can be viewed as a single convolution by the kernel $r(x, y)$, which includes both the PSF and CTI trailing. One caveat here is that the CTI kernel $c(x, y)$ in practice depends on flux, and, because a galaxy image consists of multiple pixels of varying flux, it is essential to approximate the effect with a single kernel, representing the collective effect of CTI on each galaxy.
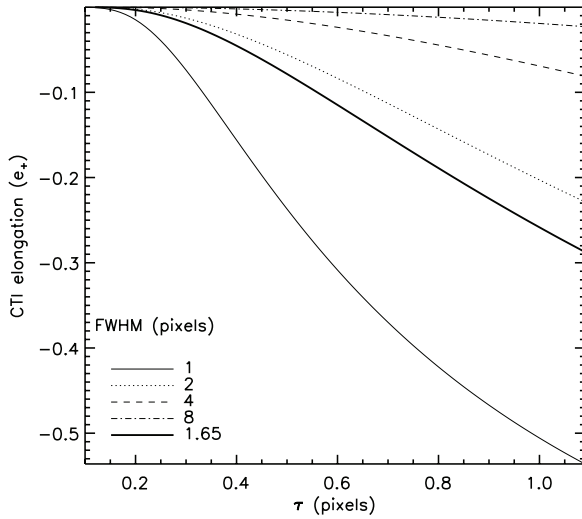
Figure 32. Time constant vs. elongation. We model the CTI trail with $\propto e^{-\tau}$, where the time constant τ determines how fast the trail truncates. The resulting ellipticity also depends on the size of the SSFs; for example, more ellipticity is induced for cosmic rays that occupy less number of pixels on average. The difference lines represent the results for different sizes. The thick solid line shows the case for the FWHM value of 1.65, which matches the mean size of the SSFs that we use for the study.

Figure 33. Galaxy shape measurement procedure with CTI and PSF corrections. (1) Surface brightness and coordinate are retrieved from the master source catalog. (2) Coordinate transformation is performed to locate the object in each visit's detector coordinate system. (3) Using the PSF model for each visit, we estimate the PSF at the object's location. (4) Based on the y-coordinate (i.e., number of charge transfer pixels) and the surface brightness, we determine the ellipticity bias (e.g., using the relation in Figure 31). Then, this ellipticity bias δe_+ is converted to the CTI time constant τ (e.g., using the relation in Figure 32). (5) The effective PSF (modified with CTI information) is rotated and scaled according to the exposure time prior to stacking for the creation of the final PSF.

One can determine the shape of the kernel $c(x, y)$ by stacking many CTI trails. We find that on average at short distances, CTI trails are well approximated by an exponential tail $\propto e^{-y/\tau}$, where the time constant τ (expressed in units of pixel) determines how quickly the trail drops. Upon close examination, however, we observe that the measured CTI trails differ in that (1) at large distances ($>$ a few pixels) the measured CTI-trail slope is shallower and (2) occasionally a couple of small bumps appear, which suggests that different species of charge traps might be present. Nevertheless, we chose the simple functional form of a single exponential because object shapes are most sensitive to the information in the central few pixels. Based on the laboratory experiments of Dawson et al. (2008), Rhodes et al. (2010) also concluded that object shapes are most sensitive to the first few pixels and a single exponential term is adequate to describe the trails.

Now the remaining question is how to determine the relation between the ellipticity bias δe_+ in the SSFs and the CTI time constant τ. For this investigation, we rely on image simulations, where we create many artificial SSFs features and trail them with the $\sim e^{-y/\tau}$ kernel. Because we select only the $r_h \sim 1$ SSFs to perform the study above, no exhaustive efforts are required to match the artificial SSFs to the real ones. Figure 32 shows the τ versus SSF ellipticity bias calibration that we derived from this image simulation. The thick solid line represents the relation when the size of the simulated SSFs matches the observed ones. The other lines illustrate how much the slope of the CTI trail depends on object sizes. The flowchart in Figure 33 summarizes the procedure to correct the PSF and CTI effects.

Although the CTI correction described here is complicated and the result of time-consuming effort, we emphasize that the effect is on average small (also perhaps negligible in many cases) for cluster lensing analysis. Figure 34 shows that very few galaxies are subject to large elongation ($\gtrsim 0.05$). A majority of galaxies, which fall to the CTI-mitigation regime are elongated by $\delta e_+ \ll 0.01$.
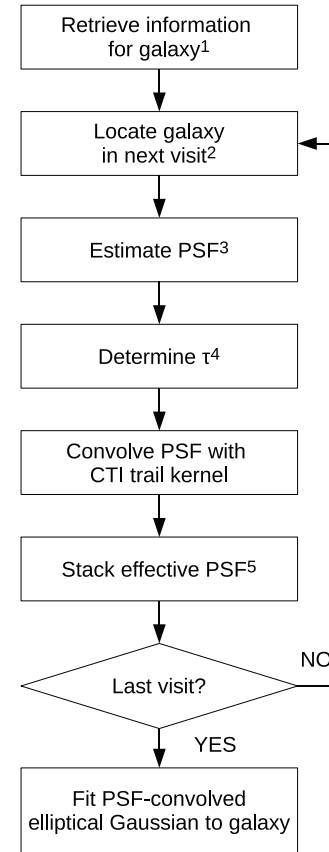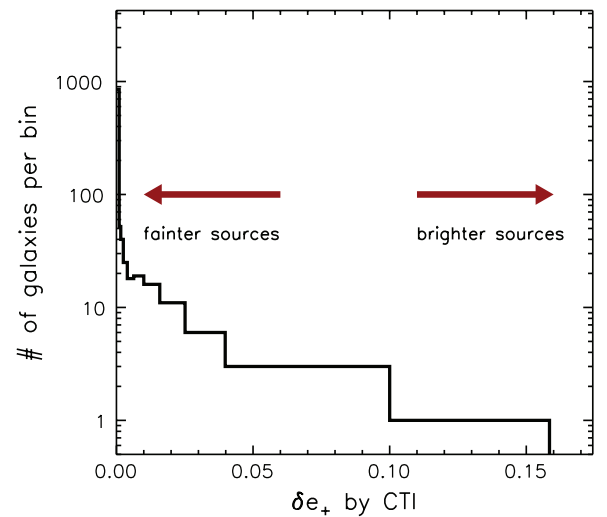

Figure 34. Number of galaxies affected by CTI elongation. We examine how many background galaxies in the ACS field are affected by a given amount of CTI elongation δe_+. Very few galaxies are subject to large elongation ($\gtrsim 0.05$). A majority of galaxies, which fall to the CTI-mitigation regime are elongated by $\delta e_+ \ll 0.01$, which can be safely ignored for cluster lensing analysis.

(A color version of this figure is available in the online journal.)

REFERENCES

Allen, S. W., Rapetti, D. A., Schmidt, R. W., Ebeling, H., Morris, R. G., & Fabian, A. C. 2008, MNRAS, 383, 879
Allen, S. W., Schmidt, R. W., & Fabian, A. C. 2001, MNRAS, 328, L37
Amanullah, R., et al. 2010, ApJ, 716, 712
Anderson, J., & Bedin, L. R. 2010, PASP, 122, 1035
Andreon, S., de Propris, R., Puddu, E., Giordano, L., & Quintana, H. 2008, MNRAS, 383, 102
Andreon, S., Trinchieri, G., & Pizzolato, F. 2011, MNRAS, 412, 2391
Andreon, S., Valtchanov, I., Jones, L. R., Altieri, B., Bremer, M., Willis, J., Pierre, M., & Quintana, H. 2005, MNRAS, 359, 1250
Arnaud, M., Pointecouteau, E., & Pratt, G. W. 2005, A&A, 441, 893
Bahcall, N. A., & Cen, R. 1993, ApJ, 407, L49
Bahcall, N. A., & Fan, X. 1998, ApJ, 504, 1
Barrientos, L. F., Gladders, M. D., Yee, H. K. C., Infante, L., Ellingson, E., Hall, P. B., & Hertling, G. 2004, ApJ, 617, L17
Bartelmann, M. 1996, A&A, 313, 697
Bertin, E., & Arnouts, S. 1996, A&AS, 117, 393
Bhattacharya, S., Heitmann, K., White, M., Lukić, Z., Wagner, C., & Habib, S. 2011, ApJ, 732, 122
Blakeslee, J. P., Anderson, K. R., Meurer, G. R., Benítez, N., & Magee, D. 2003, in ASP Conf. Ser. 295, Astronomical Data Analysis Software and Systems XII, ed. H. E. Payne, R. I. Jedrzejewski, & R. N. Hook (San Francisco, CA: ASP), 257
Blindert, K. 2006, PhD thesis, Univ. Toronto
Boehringer, H., et al. 2006, Messenger, 123, 49
Bremer, M. N., et al. 2006, MNRAS, 371, 1427
Bridle, S. L., Hobson, M. P., Lasenby, A. N., & Saunders, R. 1998, MNRAS, 299, 895
Broadhurst, T. J., & Barkana, R. 2008, MNRAS, 390, 1647
Brodwin, M., et al. 2006, ApJ, 651, 791
Brodwin, M., et al. 2011, ApJ, 732, 33
Brown, M. J. I., Dey, A., Jannuzi, B. T., Lauer, T. R., Tiede, G. P., & Mikles, V. J. 2003, ApJ, 597, 225
Bullock, J. S., Kolatt, T. S., Sigad, Y., Somerville, R. S., Kravtsov, A. V., Klypin, A. A., Primack, J. R., & Dekel, A. 2001, MNRAS, 321, 559
Cain, B., et al. 2008, ApJ, 679, 293
Coe, D., Benítez, N., Sánchez, S. F., Jee, M., Bouwens, R., & Ford, H. 2006, AJ, 132, 926
Dawson, K., et al. 2008, IEEE Trans. Nucl. Sci., 55, 1725
Dawson, K. S., et al. 2009, AJ, 138, 1271
Demarco, R., et al. 2005, A&A, 432, 381
Demarco, R., et al. 2007, ApJ, 663, 164
Duffy, A. R., Schaye, J., Kay, S. T., & Dalla Vecchia, C. 2008, MNRAS, 390, L64
Eddington, A. S. 1913, MNRAS, 73, 359
Eisenhardt, P. R., et al. 2004, ApJS, 154, 48
Eisenhardt, P. R. M., et al. 2008, ApJ, 684, 905
Elston, R. J., et al. 2006, ApJ, 639, 816
Ettori, S., Morandi, A., Tozzi, P., Balestra, I., Borgani, S., Rosati, P., Lovisari, L., & Terenziani, F. 2009, A&A, 501, 61
Evrard, A. E., et al. 2008, ApJ, 672, 122
Fahlman, G., Kaiser, N., Squires, G., & Woods, D. 1994, ApJ, 437, 56
Foley, R. J., et al. 2011, ApJ, 731, 86
Fruchter, A. S., & Hook, R. N. 2002, PASP, 114, 144
Gilbank, D. G., Gladders, M. D., Yee, H. K. C., & Hsieh, B. C. 2011, AJ, 141, 94
Gilbank, D. G., Yee, H. K. C., Ellingson, E., Hicks, A. K., Gladders, M. D., Barrientos, L. F., & Keeney, B. 2008, ApJ, 677, L89
Gioia, I. M., Maccacaro, T., Schild, R. E., Wolter, A., Stocke, J. T., Morris, S. L., & Henry, J. P. 1990, ApJS, 72, 567
Gladders, M. D., Hoekstra, H., Yee, H. K. C., Hall, P. B., & Barrientos, L. F. 2003, ApJ, 593, 48
Gladders, M. D., & Yee, H. K. C. 2005, ApJS, 157, 1
Hack, W., Busko, I., & Jedrzejewski, R. 2003, in ASP Conf. Ser. 295, Astronomical Data Analysis Software and Systems XII, ed. H. E. Payne, R. I. Jedrzejewski, & R. N. Hook (San Francisco, CA: ASP), 453
Hicks, A. K., et al. 2008, ApJ, 680, 1022
Hilton, M., et al. 2010, ApJ, 718, 133
Hoekstra, H. 2001, A&A, 370, 743
Hoekstra, H. 2003, MNRAS, 339, 1155
Hoekstra, H. 2007, MNRAS, 379, 317
Hoekstra, H., Donahue, M., Conselice, C. J., McNamara, B. R., & Voit, G. M. 2011, ApJ, 726, 48

Holden, B. P., et al. 2009, ApJ, 693, 617
Holz, D. E., & Perlmutter, S. 2010, arXiv:1004.5349
Hoyle, B., Jimenez, R., & Verde, L. 2011, Phys. Rev. D, 83, 103502
Huang, X., et al. 2009, ApJ, 707, L12
Ilbert, O., et al. 2006, A&A, 457, 841
Jee, M. J., Blakeslee, J. P., Sirianni, M., Martel, A. R., White, R. L., & Ford, H. C. 2007a, PASP, 119, 1403
Jee, M. J., & Tyson, J. A. 2009, ApJ, 691, 1337
Jee, M. J., & Tyson, J. A. 2011, PASP, 123, 596
Jee, M. J., White, R. L., Benítez, N., Ford, H. C., Blakeslee, J. P., Rosati, P., Demarco, R., & Illingworth, G. D. 2005a, ApJ, 618, 46
Jee, M. J., White, R. L., Ford, H. C., Blakeslee, J. P., Illingworth, G. D., Coe, D. A., & Tran, K.-V. H. 2005b, ApJ, 634, 813
Jee, M. J., White, R. L., Ford, H. C., Illingworth, G. D., Blakeslee, J. P., Holden, B., & Mei, S. 2006, ApJ, 642, 720
Jee, M. J., et al. 2007b, ApJ, 661, 728
Jee, M. J., et al. 2009, ApJ, 704, 672
Jenkins, A., Frenk, C. S., White, S. D. M., Colberg, J. M., Cole, S., Evrard, A. E., Couchman, H. M. P., & Yoshida, N. 2001, MNRAS, 321, 372
Jimenez, R., & Verde, L. 2009, Phys. Rev. D, 80, 127302
Kaiser, N. 1986, MNRAS, 222, 323
Kaiser, N., & Squires, G. 1993, ApJ, 404, 441
Komatsu, E., et al. 2011, ApJS, 192, 18
Lidman, C., Rosati, P., Demarco, R., Nonino, M., Mainieri, V., Stanford, S. A., & Toft, S. 2004, A&A, 416, 829
Lombardi, M., et al. 2005, ApJ, 623, 42
Mahdavi, A., Hoekstra, H., Babul, A., & Henry, J. P. 2008, MNRAS, 384, 1567
Massey, R., Stoughton, C., Leauthaud, A., Rhodes, J., Koekemoer, A., Ellis, R., & Shaghoulian, E. 2010, MNRAS, 401, 371
Maughan, B. J., Jones, L. R., Ebeling, H., & Scharf, C. 2006, MNRAS, 365, 509
Maughan, B. J., Jones, C., Jones, L. R., & Van Speybroeck, L. 2007, ApJ, 659, 1125
Mei, S., et al. 2006, ApJ, 639, 81
Meyers, et al. 2011, ApJ, submitted
Mortonson, M. J., Hu, W., & Huterer, D. 2011, Phys. Rev. D, 83, 023015
Navarro, J. F., Frenk, C. S., & White, S. D. M. 1997, ApJ, 490, 493
Papovich, C., et al. 2010, ApJ, 716, 1503
Perlman, E. S., Horner, D. J., Jones, L. R., Scharf, C. A., Ebeling, H., Wegner, G., & Malkan, M. 2002, ApJS, 140, 265
Pierpaoli, E., Stott, D., & White, M. 2001, MNRAS, 325, 77
Pierre, M., et al. 2004, JCAP, 9, 11
Press, W. H., & Schechter, P. 1974, ApJ, 187, 425
Reiprich, T. H., & Böhringer, H. 2002, ApJ, 567, 716
Rhodes, J., Leauthaud, A., Stoughton, C., Massey, R., Dawson, K., Kolbe, W., & Roe, N. 2010, PASP, 122, 439
Richmond, M. 2002, Match, Version 0.8 (Rochester: Rochester Inst. Tech.), http://spiff.rit.edu/match/
Riess, A., & Mack, J. 2004, Instrument Science Report ACS 2004-006
Rosati, P., della Ceca, R., Norman, C., & Giacconi, R. 1998, ApJ, 492, L21
Rosati, P., Stanford, S. A., Eisenhardt, P. R., Elston, R., Spinrad, H., Stern, D., & Dey, A. 1999, AJ, 118, 76
Rosati, P., et al. 2004, AJ, 127, 230
Rosati, P., et al. 2009, A&A, 508, 583
Santos, J. S., et al. 2009, A&A, 501, 49
Sartoris, B., Borgani, S., Fedeli, C., Matarrese, S., Moscardini, L., Rosati, P., & Weller, J. 2010, MNRAS, 407, 2339
Schrabback, T., et al. 2010, A&A, 516, A63
Seitz, C., & Schneider, P. 1997, A&A, 318, 687
Seitz, S., Schneider, P., & Bartelmann, M. 1998, A&A, 337, 325
Stanford, S. A., Holden, B., Rosati, P., Eisenhardt, P. R., Stern, D., Squires, G., & Spinrad, H. 2002, AJ, 123, 619
Stanford, S. A., Holden, B., Rosati, P., Tozzi, P., Borgani4, S., Eisenhardt, P. R., & Spinrad, H. 2001, ApJ, 552, 504
Stanford, S. A., et al. 2005, ApJ, 634, L129
Stanford, S. A., et al. 2006, ApJ, 646, L13
Stott, J. P., Collins, C. A., Burke, C., Hamilton-Morris, V., & Smith, G. P. 2011, MNRAS, 414, 445
Tinker, J., Kravtsov, A. V., Klypin, A., Abazajian, K., Warren, M., Yepes, G., Gottlöber, S., & Holz, D. E. 2008, ApJ, 688, 709
Tran, K.-V. H., Franx, M., Illingworth, G. D., van Dokkum, P., Kelson, D. D., Blakeslee, J. P., & Postman, M. 2007, ApJ, 661, 750
Vikhlinin, A., Kravtsov, A., Forman, W., Jones, C., Markevitch, M., Murray, S. S., & Van Speybroeck, L. 2006, ApJ, 640, 691